

SILVER NANOWIRE NETWORKS ON POLYDIMETHYLSILOXANE FOR
ORGANIC AND PEROVSKITE SOLAR CELL ELECTRODES

A THESIS SUBMITTED TO
THE GRADUATE SCHOOL OF NATURAL AND APPLIED SCIENCES
OF
MIDDLE EAST TECHNICAL UNIVERSITY

BY

ELIF ÖZLEM GÜNER

IN PARTIAL FULFILLMENT OF THE REQUIREMENTS
FOR
THE DEGREE OF MASTER OF SCIENCE
IN
METALLURGICAL AND MATERIALS ENGINEERING

SEPTEMBER 2019

Approval of the thesis:

**SILVER NANOWIRE NETWORKS ON POLYDIMETHYLSILOXANE FOR
ORGANIC AND PEROVSKITE SOLAR CELL ELECTRODES**

submitted by **ELIF ÖZLEM GÜNER** in partial fulfillment of the requirements for
the degree of **Master of Science in Metallurgical and Materials Engineering**
Department, Middle East Technical University by,

Prof. Dr. Halil Kalıpçılar
Dean, Graduate School of **Natural and Applied Sciences**

Prof. Dr. C. Hakan Gür
Head of Department, **Met. and Mat. Eng.**

Prof. Dr. H. Emrah Ünalın
Supervisor, **Met. and Mat. Eng., METU**

Examining Committee Members:

Prof. Dr. Ali Çırpan
Chemistry Dept, METU

Prof. Dr. H. Emrah Ünalın
Met. and Mat. Eng., METU

Assoc. Prof. Dr. Görkem Günbař
Chemistry Dept, METU

Assist. Prof. Dr. Selçuk Yerci
Micro and Nanotechnology Dept, METU

Assist. Prof. Dr. řahin Cořkun
Met. and Mat. Eng. Dept, Eskiřehir Osmangazi University

Date: 05.09.2019

I hereby declare that all information in this document has been obtained and presented in accordance with academic rules and ethical conduct. I also declare that, as required by these rules and conduct, I have fully cited and referenced all material and results that are not original to this work.

Name, Surname: Elif Özlem Güner

Signature:

ABSTRACT

SILVER NANOWIRE NETWORKS ON POLYDIMETHYLSILOXANE FOR ORGANIC AND PEROVSKITE SOLAR CELL ELECTRODES

Güner, Elif Özlem
Master of Science, Metallurgical and Materials Engineering
Supervisor: Prof. Dr. H. Emrah Ünalın

September 2019, 68 pages

Transparent and conductive electrodes are widely used in optoelectronic devices. The most prominent and commercial transparent conductive electrode is indium tin oxide (ITO). However, there is an increasing demand to replace ITO with alternative materials due to inherent drawbacks of ITO such as its cost, brittleness and scarcity of indium. Silver nanowire (Ag NW) networks are among the best candidates to replace ITO with their excellent optoelectronic and mechanical properties. Ag NW networks have already been demonstrated as electrodes in a wide range of applications such as transparent heaters, flexible displays, stretchable electronics and photovoltaic devices. However, there are still some challenges in obtaining a uniform Ag NW network on different substrates. In this thesis, a polydimethylsiloxane (PDMS) assisted transfer method was developed to overcome this problem. Ag NWs synthesized via polyol process were spray coated onto glass substrates in network form. PDMS was then casted onto Ag NW networks and peeled off following curing to transfer Ag NWs onto PDMS surface. This transparent Ag NW embedded PDMS substrates were then used as electrodes in both organic and perovskite based solar cells. First, a semi-transparent organic solar cell (OSC) with Ag NW/PDMS electrodes was demonstrated using a commercially available and a novel polymer as the photoactive layers. Power conversion efficiencies of above 2% and 3% was obtained from these cells with

architectures of glass/ITO/ZnO/P3HT:PCBM/PEDOT:PSS/Ag NW/PDMS and glass/ITO/ZnO/PBDB-T:ITIC/PEDOT:PSS/Ag NW-PDMS, respectively, under AM 1.5G illumination conditions. Secondly, a mesoporous perovskite solar cell was demonstrated using Ag NW/PDMS electrodes and commercially available photoactive layers. The cells based on glass/FTO/k-TiO₂/m-TiO₂/Perovskite/Spiro-OMeTAD/Ag NW/PDMS architecture showed a power conversion efficiency of 6.5% under AM 1.5G illumination conditions. PDMS assisted transfer method utilized herein offers a simple, solution-based and transparent alternative to evaporation method for the formation of solar cell electrodes.

Keywords: Silver nanowire networks, transparent conducting electrodes, organic solar cells, perovskite solar cells

ÖZ

POLİDİMETİLSİLOKSAN ÜZERİNDEKİ GÜMÜŞ NANOTEL İNCE FİMLERİN ORGANİK VE PEROVSKİT GÜNEŞ HÜCRELERİNDE ELEKTROT OLARAK UYGULANMASI

Güner, Elif Özlem
Yüksek Lisans, Metalurji ve Malzeme Mühendisliği
Tez Danışmanı: Prof. Dr. H. Emrah Ünalın

Eylül 2019, 68 sayfa

Şeffaf ve iletken elektrotlar optoelektronik cihazlarda yaygın olarak kullanılmaktadır. Bu alanda en önde gelen ticari şeffaf ve iletken elektrot indiyum kalay oksittir (ITO). Fakat ITO'nun fiyat ve kırılgenliğinin yanısıra indiyumun az bulunurluğu gibi dezavantajlarından dolayı, ITO'ya alternatif bir elektrot malzemesi bulunması için giderek artan bir talep bulunmaktadır. Üstün optoelektronik ve mekanik özellikleri sebebiyle gümüş nanoteller, ITO'ya alternative malzemeler olarak görülmektedir. Günümüze kadar gümüş nanotel ağları, şeffaf ısıtıcılar, esnek ekranlar, gerdirilebilir elektronik cihazlar ve fotovoltaik cihazlar gibi pek çok uygulamada kullanılmıştır. Ancak, gümüş nanotellerin kimi alttaşlar üzerinde eş dağılımlı kaplanmasında bazı sorunlar çıkmaktadır. Bu tezde, bahsi geçen kaplama sorunlarının üstesinden gelmek için polidimetilsiloksan (PDMS) destekli aktarım yöntemi geliştirilmiştir. Polyol metodu ile sentezlenen gümüş nanoteller cam alttaşlar üzerine püskürtmeli kaplama yöntemi ile ince film oluşturacak şekilde kaplanmıştır. PDMS polimerinin gümüş nanotel ince filmlerin üzerine kaplanmasının ardından cam alttaşların yüzeyinden ayırarak gümüş nanotellerin PDMS yüzeyine aktarımı sağlanmıştır. Elde edilen gümüş nanotel gömülü şeffaf PDMS alttaşlar, hem organik hem de perovskit güneş hücrelerinde elektrot olarak kullanılmıştır. İlk olarak, hem piyasada bulunan hem de

özgün polimerlerden üretilen fotoaktif katmanlara sahip, yarı şeffaf organik güneş hücreleri, gümüş nanotel/PDMS elektrotlar ile gerçekleştirilmiştir. Cam/ITO/ZnO/P3HT:PCBM/PEDOT:PSS/gümüş nanotel/PDMS ve Cam/ITO/ZnO/PBDB-T:ITIC/PEDOT:PSS/gümüş nanotel/PDMS mimarisindeki cihazlar ile sırasıyla %2 üzeri ve %3 üzeri güç dönüşüm verimleri AM 1.5G aydınlatma koşulları altında elde edilmiştir. İkinci olarak, bir mezogözenekli perovskit güneş hücresi gümüş nanotel/PDMS elektrotlar ve piyasada bulunan fotoaktif katmanlar kullanılarak üretilmiştir. Cam/FTO/k-TiO₂/m-TiO₂/Perovskit/Spiro-OMeTAD/gümüş nanotel/PDMS mimarisindeki cihazlar ile %6.5 güç dönüşüm verimi elde edilmiştir. Burada kullanılan PDMS destekli aktarım yöntemi, güneş hücrelerinin elektrotlarını oluşturmak için kullanılan buharlaştırma yöntemine basit, çözeltiye dayalı ve şeffaf bir alternatif sunmaktadır.

Anahtar Kelimeler: Gümüş nanotel ince filmler, şeffaf ve iletken elektrotlar, organik güneş hücreleri, perovskite güneş hücreleri

To my late grandfather

ACKNOWLEDGEMENTS

This thesis was financially supported by The Scientific and Technological Research Council of Turkey (TÜBİTAK) under grant numbers 115M036 and 315M360, and by Middle East Technical University, Scientific Research Projects Program under project number YLT-308-2018-3736.

Firstly, I would like to thank Prof. Dr. H. Emrah Ünalan for his support and guidance throughout this study. He has been encouraging all the time and given me chances to work for several projects. I am very grateful for working under his supervision. I also would like to thank Dr. Şahin Coşkun for his guidance and academic knowledge that he delivered to me.

I am thankful to my lab mates Doğa Doğanay, Serkan Koylan, Mete Batuhan Durukan, Alptekin Aydın, Yusuf Tutel, Şensu Tunca, Merve Nur Güven, Almira Çaldıkoğlu and Şeyma Koç. I am also thankful to Ece Alpugan for sharing her knowledge and experience with me. I would like to thank Gönül Hızalan and Hava Akpınar for their collaboration and guidance. A parenthesis for Umutcan Ertürk shall be opened. Thank you for all.

I would like to express my deepest gratitude to Berkay Bayramin. Thank you for supporting me always and being there for me throughout all the hardest times. I felt your support in every step that I had taken. Thank you for everything. I love you.

I am grateful to Havva Nur Tümbaş for her intimate friendship. We have shared almost every moment in our lives along 10 years. I am also thankful to Aşina Pamuk and Mustafa Balcılar for all the fun and sharing through this period. They have always backed me up. Also, I would like to thank my dear friend and lab mate İpek Bayraktar for her never-ending social and academic support.

Lastly, I would like to thank my family Sevginar Güner, Ramis Güner, Fatih Güner and Arzu Doğaner. They have never lost their support and faith on me.

TABLE OF CONTENTS

ABSTRACT	v
ÖZ	vii
ACKNOWLEDGEMENTS.....	x
TABLE OF CONTENTS	xii
LIST OF TABLES.....	xv
LIST OF FIGURES	xvi
LIST OF ABBREVIATIONS.....	xix
LIST OF SYMBOLS	xxi
CHAPTERS	
1. INTRODUCTION.....	1
2. TRANSPARENT AND CONDUCTING SILVER NANOWIRE/PDMS ELECTRODES.....	5
2.1. Introduction.....	5
2.1.1. Conventional Transparent Electrode Materials.....	5
2.1.2. Alternative Transparent Electrode Materials	6
2.1.2.1. Graphene.....	6
2.1.2.2. Carbon Nanotubes (CNTs)	7
2.1.2.3. Conductive Polymers.....	8
2.1.2.4. Metal Grids	8
2.1.2.5. Metal Nanowires.....	9
2.2. Silver Nanowires.....	12
2.3. Experimental Details.....	19

2.3.1. Synthesis of Silver Nanowires	20
2.3.2. Fabrication of Ag NW/PDMS Electrodes	20
2.4. Characterization Methods.....	22
2.4.1. SEM Analysis	22
2.4.2. Transparency Measurements	22
2.4.3. Sheet Resistance Measurements	22
2.4.4. AFM Measurements	22
2.5. Results	22
3. TRANSPARENT AND CONDUCTING Ag NW/PDMS ELECTRODES FOR ORGANIC SOLAR CELLS	29
3.1. Introduction	29
3.2. Device Architecture and Operation Principles	29
3.3. Silver Nanowire Networks as Transparent Conducting Electrodes for Organic Solar Cells	36
3.4. Experimental Details	38
3.4.1. Fabrication of Ag NW/PDMS Top Electrodes	38
3.4.2. Fabrication of Inverted Solar Cells.....	39
3.5. Characterization Methods.....	42
3.5.1. Scanning Electron Microscopy (SEM).....	42
3.5.2. Atomic Force Microscopy (AFM).....	42
3.5.3. Transmittance Measurements	42
3.5.4. Current – Voltage Characteristics.....	42
3.6. Results	42
4. TRANSPARENT AND CONDUCTING Ag NW/PDMS ELECTRODES FOR PEROVSKITE SOLAR CELLS	51

4.1. Introduction.....	51
4.2. Device Architecture and Operation Principles.....	51
4.3. Experimental Details.....	53
4.3.1. Fabrication of Perovskite Solar Cells.....	53
4.3.2. Fabrication of Ag NW/PDMS Electrodes.....	54
4.4. Characterization Methods.....	54
4.4.1. Scanning Electron Microscopy (SEM).....	54
4.4.2. Photovoltaic Characterization.....	55
4.5. Results.....	55
5. CONCLUSIONS AND FUTURE RECOMMENDATIONS.....	59
5.1. Conclusions.....	59
5.2. Future Recommendations.....	60
REFERENCES.....	61

LIST OF TABLES

TABLES

Table 2. 1 FoMs of Ag NW, Ag NW/PDMS, ITO and FTO thin films.....	26
Table 3. 1 Materials used in normal and inverted geometries and their roles [62]. ..	31
Table 3. 2 Performance of solar cells with electrodes having different sheet resistances.	45
Table 3. 3 Photovoltaic parameters of IOSCs with Ag NW/PDMS and Au anode. .	46
Table 3. 4 Photovoltaic parameters of glass/ITO/ZnO/P3HT:ICBA/PEDOT:PSS/Ag NW-PDMS structured IOSC.....	48
Table 3. 5 Photovoltaic parameters of glass/ITO/ZnO/PBDB-T:ITIC/PEDOT:PSS/Ag NW-PDMS structured solar cell device.....	50

LIST OF FIGURES

FIGURES

- Figure 2. 1** (a) Optical transmittance, haze factor, FoMs, sheet resistance vs areal mass density. (b) Transmittance with respect to sheet resistance for several TCEs including dashed lines showing FoMs. (c) Transmittance comparison of bare glass, Ag NWs and FTO, all of which have the same sheet resistance of $\sim 11 \Omega/\text{sq}$. (d) Dependence of haze factor to FoMs for Ag NW networks [34]. 11
- Figure 2. 2** Schematic representation of the synthesis process (a) formation of a nanorod from an MTP. (100) surfaces are confined with PVP and (111) facets left as active sites for Ag atom accumulation. (b) addition of Ag atoms on (111) surfaces (shown by arrows) and anisotropic growth of a nanowire into [110] direction [47]. 13
- Figure 2. 3** SEM images of as-deposited Ag NW network (a) and (c) and annealed at 200°C for 20 minutes (b) and (d) [47]. 15
- Figure 2. 4** (a) Schematics of PDMS transfer process, (b) Transferred Ag NW network on PET substrate, (c) Transferred Ag NW network on glass substrate, (d) The flexibility of the film on PET, (e) Adhesion test results of transferred Ag NW film, tape is peeled from the region between the dotted lines and Ag NWs still remain on the surface, (f) to (i) SEM images of top, left, bottom and top of the transferred film showing the uniformity, respectively [49]. 16
- Figure 2. 5** (a) Sheet resistance vs transmittance curves of annealed and as-received samples. (b) SEM image showing fusion of a junction [49]. 17
- Figure 2. 6** Schematics showing (a) Spray coating on a patterned PDMS stamp, (b) Transfer of pixelated Ag NW thin film on a receiver substrate, (c) Photo of the patterned sample and (d) SEM image of Ag NW thin film obtained from a pixel [50]. 18
- Figure 2. 7** SEM images of composite electrode (a) top view, (b) cross-sectional view, (c) Angled cross-sectional view, (d) Angled cross-sectional view at a higher

magnification, (e) AFM image of composite electrode surface and height profile of a nanowire. The nanowire used for height profile is marked with a blue box on AFM image [3].	19
Figure 2. 8 Photographs of (a) Ag NWs dispersed in ethanol and (b) spray deposition of Ag NWs onto glass substrates via airbrush.	21
Figure 2. 9 SEM image of purified Ag NWs.	23
Figure 2. 10 (a) Diameter and (b) length distribution of Ag NWs used in this work.	23
Figure 2. 11 Different magnification SEM images of glass substrate after transfer of Ag NW network at magnifications of (a) 40000X, (b) 20000X and (c) 10000X.	24
Figure 2. 12 Transmittance curves of Ag NW and Ag NW/PDMS electrodes with sheet resistances of (a) 10, (b) 25 and (c) 50 Ω /sq, (d). Transmittance curve for bare PDMS.	25
Figure 2. 13 Transmittance curves for Ag NW network with different sheet resistances	27
Figure 2. 14 Transmittance curves for Ag NW/PDMS with different sheet resistances	27
Figure 2. 15 AFM images of Ag NW/PDMS electrodes showing (a) phase image, (b) 3D image and bare PDMS showing (c) phase image and (d) 3D image, respectively.	28
Figure 3. 1 BHJ OSC devices with (a) normal geometry and (b) inverted geometry [62].	31
Figure 3. 2 Energy diagram of donor acceptor interface [68].	32
Figure 3. 3 (a) Schematic representation of photocurrent generation in terms of photon absorption, exciton generation, exciton dissociation and charge carrier collection, (b) schematic diagram of charge carrier transportation in photoactive material of a BHJ device [62].	34
Figure 3. 4 Typical J-V curve of an OSC [62].	35
Figure 3. 6 Schematic illustration of bottom contact.	39
Figure 3. 6 Schematic top view of fabricated devices.	41

Figure 3. 7	SEM image of Ag NW/PDMS electrodes.....	43
Figure 3. 8	Schematic view of the fabricated devices (a) side-view, photos of (b) Ag NW/PDMS electrode and (c) inverted OSC with Ag NW/PDMS top electrode.	44
Figure 3. 9	J-V curve of glass/ITO/ZnO/P3HT:PCBM/PEDOT:PSS/Ag NW-PDMS (20 Ω /sq) structured IOSC.....	45
Figure 3. 10	J-V curve of glass/ITO/ZnO/P3HT:PCBM/PEDOT:PSS/Au structured IOSC.	46
Figure 3. 11	(a) Schematic view, (b) photo of Glass/ITO/ZnO/P3HT:ICBA/PEDOT:PSS/Ag NW-PDMS devices.	47
Figure 3. 12	J-V curve of glass/ITO/ZnO/P3HT:ICBA/PEDOT:PSS/Ag NW-PDMS structured IOSC.	48
Figure 3. 13	(a) Schematic view and (b) photo of glass/ITO/ZnO/PBDB-T:ITIC/PEDOT:PSS/Ag NW-PDMS device.....	49
Figure 3. 14	J-V curve of glass/ITO/ZnO/PBDB-T:ITIC/PEDOT:PSS/Ag NW-PDMS structured solar cell device.	49
Figure 4. 1	Device structure of PSCs having (a) normal mesoscopic, (b) normal planar, (c) inverted planar and (d) inverted mesoscopic geometries [71].	52
Figure 4. 2	(a) SEM image of Ag NW/PDMS electrodes, Photographs of (b) Ag NW/PDMS electrodes, (c) Perovskite solar cell.....	55
Figure 4. 3	Schematic illustration of device architecture	56
Figure 4. 4	J-V curve of control device	56
Figure 4. 5	J-V curve of perovskite solar cell with Ag NW/PDMS cathode.....	57

LIST OF ABBREVIATIONS

1D	One dimensional
2D	Two dimensional
AAO	Anodic aluminum oxide
AMD	Areal mass density
AZO	Aluminum doped tin oxide
BHJ	Bulk heterojunction
CdTe	Cadmium telluride
CIGS	Copper indium-gallium selenide
CNT	Carbon nanotubes
CVD	Chemical vapor deposition
EG	Ethylene glycol
FF	Fill factor
FoMs	Figures of merit
FTO	Fluorine doped tin oxide
GaAs	Gallium arsenide
GMST	Global mean surface temperature
HCl	Hydrochloric acid
HOMO	Highest occupied molecular orbital
HTL	Hole transport layer
ICBA	Indene-C60 bisadduct
IOSC	Inverted organic solar cell
ITO	Indium tin oxide
Jsc	Short circuit current
LCD	Liquid crystal display
LUMO	Lowest unoccupied molecular orbital
MoO₃	Molybdenum oxide
MTP	Multi-twinned particles
MWCNT	Multi walled carbon nanotube
NaCl	Sodium Chloride
NiO	Nickel oxide
NP	Nanoparticle
OLED	Organic light emitting diode
OSC	Organic solar cell
P3HT	Poly(3-hexylthiophene)
PBDTT-DPP	Poly(2,6-(4,8-bis(5-ethylhexylthiophenyl)benzo-[1,2-b;3,4-b]dithiophene-alt-5-dibutyl-octyl-3,6-bis(5-bromothiophen-2-yl)pyrrolo[3,4-c]pyrrole-1,4-dione)
PC₆₁BM	Phenyl-C61-butyric acid methyl ester
PC₇₁BM	Phenyl-C71-butyric acid methyl ester

PCE	Power conversion efficiency
PDMS	Polydimethylsiloxane
PEDOT:PSS	Poly(3,4 ethylenedioxythiophene)-poly(styrenesulfonate)
PEN	Polyethylene naphthalate
PES	Polyether sulfone
PET	Polyethylene terephthalate
PLED	Polymer light emitting diode
PSC	Perovskite solar cell
PTFE	Polytetrafluoroethylene
PV	Photovoltaic
PVP	Polyvinyl pyrrolidone
R_s	Series resistance
R_{SH}	Shunt resistance
SPP	Surface plasmon polarions
SWCNT	Single walled carbon nanotube
TCE	Transparent conductive electrodes
TFT	Thin film transistors
TiO_x	Titanium oxide
V₂O₅	Vanadium oxide
V_{oc}	Open circuit voltage
ZnO	Zinc oxide

CHAPTER 1

INTRODUCTION

The energy consumption of today's world heavily relies on fossil fuels such as coal, oil and natural gas. Fossil fuels are not renewable energy sources, as their formation takes millions of years. As they are being used, the finite sources of these fossil fuels begin to diminish. As a result of scarcity in fossil fuel sources, it becomes struggling and expensive to sustain extraction processes. In addition, utilization of fossil fuels for energy demand causes global warming. Combustion of fossil fuels increases the greenhouse gas emissions, which pollutes the air, puts public health in danger and increases the global mean surface temperature (GMST). According to IPCC Special Report, GMST increased 1.0 °C as compared to pre-industrial levels and it might reach to 1.5 °C between 2030 – 2052 if the increasing trend continue. The increase in GMST has critical effects on the nature, ecosystems and public health. Increased poverty, degradation of certain geographical sites, loss of certain terrestrial lands, changed ocean acidity and changed marine ecosystems, increased epidemic diseases, increased rate of propagation of epidemics, increased probability of natural disasters are the most possible results of global warming [1]. At this point, renewable energy sources become prominent due to being less harmful for the nature, more sustainable and cost-effective. Renewable energy sources including solar, wind, biomass, geothermal and hydropower energy cannot be depleted since they are based on nature. Among them, solar energy is the well-known and vastly utilized energy source. It is also the biggest energy source for the earth. Thus, harnessing solar energy was a long – term objective for many scientists. In 1954, Bell Labs developed the first silicon photovoltaic (PV) cell [2]. A solar cell is a device, which converts the energy of the incident light to electricity. When the light shines on the solar cell, an electron is excited to higher energy levels. The excited electron travels through the cell and reaches to an external

circuit. After dissipating its energy to the external circuit, the electron goes back to the cell. In order to enhance the performance of the solar cells a wide variety of materials and concepts are developed.

Thin film materials combining high electrical conductivity and high optical transmittance are used in many electronic devices such as liquid crystal displays (LCDs), organic light emitting diodes (OLEDs), touch panels, smart glasses, e-paper and solar cells. Vast amount of thin film studies depends on transparent conductive electrodes (TCEs) such as indium doped tin oxide (ITO), fluorine doped tin oxide (FTO), aluminum doped zinc oxide (AZO). ITO is the most commonly utilized TCE material due to its high electrical conductivity and high optical transmittance. However, high-quality ITO thin films are produced via a high vacuum process. Either during or after production, they require a high temperature processing step, which is increasing the production costs and also limiting the deposition of ITO onto polymers. On the other hand, indium is a scarce element, which increases the cost of the ITO thin films. Another drawback of ITO is its brittleness, which prevents its utilization in flexible or stretchable applications. Therefore, flexible, stretchable, low – cost, low – temperature processed, alternative conductive coatings are required. Graphene, carbon nanotubes (CNTs), conductive polymers, metallic grids and metal nanowires are the most promising alternative material groups. Most of these materials cannot compete with the performance of transparent oxides. Especially, solution – processed carbon-based materials have quite high sheet resistance values like 100 to 5000 Ω /sq as compared to TCEs when the two groups have similar optical transmittance values [3]. Metallic nanowires, on the other hand, are realized as potential alternative conductive thin films competing with ITO. Since bulk silver has the highest electrical conductivity, it is also highly promising in nanowire form. In addition, when used in network form that is percolating, the optoelectronic properties of those networks are better than that of ITO. Moreover, these networks can withstand stretching forces, which makes nanowires and silver nanowires in particular, good candidates for flexible electronics. Coşkun et al. showed that Ag NWs can replace ITO for anodes of

polymer light emitting diodes (PLEDs) [4]. Roughness being the biggest problem for Ag NW networks can be solved by thermal annealing and coating with a conductive polymer. After coating with poly(3,4 ethylenedioxythiophene)-poly(styrenesulfanate) (PEDOT:PSS), the rough mean square (RMS) roughness values decreased significantly. Utilization of Ag NW networks as transparent heaters are also highly investigated in literature [5]–[8]. Ag NW networks have shown outstanding performance due to their excellent optoelectronic properties and reached high temperatures through the application of lower voltages as compared to other transparent conducting materials. Front electrodes of solar cells [9]–[11], displays (OLEDs) [12], capacitive touch sensors [13] are the other application areas that intensively make use of Ag NWs. Lastly, Ag NWs synthesized with subwavelength diameter and high uniformity lead to the formation of surface plasmon polaritons (SPPs) at certain optical frequencies and are benefitted for the production of plasmonic waveguides [14].

In this thesis, a novel PDMS assisted transfer method was developed. Fabrication of TCEs by embedding Ag NWs into polydimethylsiloxane (PDMS) substrates was studied (Chapter 2). Their optical and electrical properties were systematically investigated. Then, Ag NW/PDMS electrodes were utilized as top electrodes for organic solar cells (Chapter 3). Their effect on the device performance was investigated. Lastly, Ag NW/PDMS electrodes were utilized as top electrodes for perovskite solar cells (Chapter 4). The applicability of transparent and conductive Ag NWs/PDMS thin films as top electrodes in perovskite solar cells was examined.

CHAPTER 2

TRANSPARENT AND CONDUCTING SILVER NANOWIRE/PDMS ELECTRODES

2.1. Introduction

TCEs are thin film materials having both high optical transparency and high electrical conductivity. Many optoelectronic devices like solar cells, touch screens, sensors, transparent heaters, OLEDs, LCDs and smart windows require the utilization of high-quality thin film materials. In the last two decades, large number of studies were conducted on TCE materials.

2.1.1. Conventional Transparent Electrode Materials

ITO is the most commonly used TCE material with a sales figure of 1.6 billion \$ in 2013 [12]. High optical transparency ($>90\%$ at a wavelength of 550 nm) at low sheet resistance ($\sim 10 \Omega/\text{sq}$) make ITO a very attractive material for transparent electrode applications. Being chemically stable and having abrasion resistance are the other advantages of ITO. However, there are some attributes which drive scientists to investigate alternatives to ITO. Indium element is very scarce on earth's crust (0.05 ppm), thus its price is continuously increasing [15]. Moreover, ITO is a crystalline ceramic material, which makes it inherently brittle and highly incompatible with flexible substrates. The production of ITO requires high vacuum processes like sputtering and also high temperature post processes. Thus, the production costs are quite high. Besides, production of highly conductive ($<10 \Omega/\text{sq}$) ITO is more expensive than the production of low conductivity ITO. This is because the sheet resistance of ITO decreases with an increase in thickness. Likewise, as the thickness increases, the rate of film throughput decreases in sputtering processes. That in turn increases the cost of the thicker, high-conductivity material. For example, for solar

cell applications in which ITO on PET electrodes are utilized, up to 51% of the total price can come from ITO [16]. Other than ITO, FTO and AZO are prominent TCE materials, yet they have similar drawbacks. Therefore, tremendous efforts have been spent on the development of alternative TCE thin films.

2.1.2. Alternative Transparent Electrode Materials

In the few past years, considerable amount of work was dedicated to develop potential alternative transparent electrode materials. Although the properties are highly application dependent, flexibility, chemical stability, process ease, low cost, electrical and optical properties are primarily concerned. In this regard, the most promising alternative TCEs are graphene, carbon nanotubes (CNTs), conductive polymers, metallic grids and metallic nanowires [17]–[19].

2.1.2.1. Graphene

Graphene is a two dimensional and one atomic layer thick, zero bandgap material composed of carbon atoms. Due to being zero bandgap and having sp^2 hybridization, its delocalized charge carriers enable charge transport in a planar manner. Due to its unique electronic structure, a pure single layer graphene has a Fermi velocity $V_F = 10^6$ m/s, which results in a high electrical conductivity [20]. Graphene was primarily produced from exfoliating graphite using a scotch tape in 2004 [21]. However, this method was not compatible with large scale manufacturing techniques. Thus, scientist developed alternative production techniques such as solution – processing methods and chemical vapor deposition (CVD). Size of solution processed graphene flakes are very small and therefore for forming a network many of these graphene flakes should come together as a patchwork. The main drawback of solution processed graphene networks is quite high values of sheet resistance due to the grain boundaries between the graphene flakes and the internal defects. In addition, it is very difficult to get graphene down to a monolayer and therefore the optical transmittance values are relatively high. Typically, the sheet resistance and transparency of solution-processed graphene networks are $\sim 2000 \Omega/\text{sq}$ and 85%, respectively [18]. On the other hand,

CVD is a promising technique for the production of graphene networks since it can provide lower sheet resistance and transparency, which are 700 Ω/sq and 90%, respectively [18]. Although CVD method is expensive and not compatible with large scale manufacturing, it still has an important role in the production of single layer and almost defect-free graphene.

2.1.2.2. Carbon Nanotubes (CNTs)

Carbon nanotubes are tubes of graphite sheets that consists of carbon atoms arranged in a hexagonal manner. They can be made up of a single layer of carbon atoms, called as single-walled carbon nanotubes (SWCNTs) or many concentrically placed layers, called as multi-walled carbon nanotubes (MWCNTs). Hexagonal network of sp^2 hybridized carbon sheets can be arranged in different ways around the tube axis, which is called as tube chirality. SWCNTs can either behave like semiconductors or metals depending on the chirality. Metallic SWCNTs have very high conductivities like 10^5 S/cm [22]. Moreover, metallic SWCNTs absorb light in a broad range as bulk metals do whereas semiconducting SWCNTs are transparent to visible light. The strong van der Waals forces between nanotubes make the dispersion of CNTs and fabrication of homogenous CNT films difficult. Thin films of CNTs are used as transparent electrodes in various types of electronic devices like OLEDs and thin film transistors (TFTs) [23], [24]. Although a single CNT has superior electrical properties, a network of CNTs result in a very high sheet resistance. This is due to the high resistance occurring at the junctions of these nanotubes. In order to overcome this problem, different techniques were developed such as acidic treatments and surface modifications [25]. On the other hand, CNTs are compatible with roll-to-roll production methods, which have a key role in large-scale manufacturing Yet, the challenges in the synthesis, purification and post-processing steps increase the cost of the material and prevent the replacement of ITO with CNTs.

2.1.2.3. Conductive Polymers

Utilization of conductive polymers as transparent and conductive electrodes in various optoelectronic devices has been investigated over the past decades. They have alternating σ and π bonds in their structure and these conjugated π bonds provide delocalized charge carriers through the backbone of the polymer. Among various types of conductive polymers, the mostly utilized one is PEDOT:PSS. Transparency in thin film form, flexibility, solution processability and low-cost are the main advantages of PEDOT:PSS. However, the electrical conductivity of PEDOT:PSS is remarkably low [22]. To enhance the conductivity, oxidative doping of PEDOT:PSS is practiced [26]. Unfortunately it is revealed that, this conductivity can decrease when the material is exposed to high temperatures, humidity or UV light [27]. The instability in its electrical states prevent the large-scale utilization of PEDOT:PSS as an electrode material. On the other hand, its work function changes between 4.7 eV and 5.4 eV which makes PEDOT:PSS a suitable hole injection and hole transport layer on the anode in OLED and solar cell applications [27].

2.1.2.4. Metal Grids

High work function metals like Au, Al and Ag are extensively used as electrode materials due to their excellent conductivity. However, if the film thickness is greater than 10 nm, the thin film loses its transparency. Other option to benefit high conductivity with optical transparency within metals is to pattern thin metallic films into metal grids or meshes. Thus, the passage of the light is allowed through the holes of the grid, which enables high optical transmission between the grid lines. Electrical conductivity and optical transmittance can be tuned by changing the dimensions of the grid structure. Zou et al., reported a sheet resistance and optical transmittance of 9.1 Ω/sq and 79%, respectively, upon adjusting the pattern size [28]. These grids can be fabricated via various elaborated techniques including nanoimprint lithography, direct laser interference patterning, electro-hydro-dynamic printing, [22], inkjet printing [29] and crack templating [30]. Roll-to-roll printing is another method enabling the large-

scale manufacturing of metal grids. The biggest drawback of metal grids is that their roughness is quite high. High surface roughness causes shorts in devices and also prevents the formation of a good interfacial matching between the electrode and the underlying layer.

2.1.2.5. Metal Nanowires

Another approach to benefit high electrical conductivity and optical transparency of metals is fabricating metal nanowire thin films. Typically, a nanowire has the dimensions of ~40-200 nm in diameter and several microns in length. The increased aspect ratio improves electrical, optical and mechanical properties of metal nanowire thin films. Metal nanowire thin films can compete with ITO in terms of optoelectronic properties and compatibility with flexible substrates and devices. Metallic nanowires can be grown via solution-based methods and can then be deposited onto substrates in thin film form via several different methods. They are suitable for large-scale manufacturing techniques. Moreover, nanowires with high aspect ratio easily percolate in thin film form thus thin films necessitate the use of less amount of nanowires. Ag, Cu and Au nanowires are the most commonly investigated and utilized metallic nanowires. Among them, Ag NW networks are the strongest competitor to ITO in terms of their optoelectronic properties, stability and cost [31].

Optoelectronic properties of metallic nanowire thin films are highly dependent on the nanowire size. As the diameter of a nanowire decreases near to its electron mean free path, its electrical resistivity increases significantly due to increasing surface scattering of electrons [32]. Smaller nanowire diameters, on the other hand, are beneficial in terms of optical transmittance but are less stable environmentally. As the diameter of a nanowire increases, the number of photons scattered from the nanowire surface increases leading to decreasing transmittance in thin film form. Moreover, larger diameter nanowires increase the surface roughness in thin film form, which is an undesired attribute for some devices such as organic solar cells (OSCs) and OLEDs.

On the other hand, longer nanowires improve the optical transmittance of thin films due to having less junction points in unit area. In parallel, surface roughness of the network can be decreased with longer nanowires since conductive paths are formed with less number of nanowire junctions.

Network density is another important parameter used for defining the optoelectronic properties of metallic nanowire thin films. It is usually referred to as areal mass density (amd). There is a mathematical relationship between network density and optoelectronic properties of thin films. Optical transmittance decreases with amd whereas electrical resistivity decreases by power law. Increasing nanowire density decreases the sheet resistance of the thin films and also decrease the optical transmittance. Therefore, there is always a trade-off between transparency and sheet resistance. Yet, the biggest advantage of MNWs is the ability to accomplish lower sheet resistances and the optical transmittance in a broad range of spectrum including visible and near infrared regions.

The performance assessment of TCEs are carried out by utilizing figures of merit (FoMs). A classical definition of FoMs was realized by Haacke in 1976 as the following [33]

$$FoM = \frac{T^{10}}{R_s}$$

, where T is the optical transmittance at 550 nm and R_s is the sheet resistance. Besides, there is another FoMs expression as the following [31]

$$FoM = \frac{\sigma_{DC}}{\sigma_{Op}}$$

, where σ_{DC} is the DC conductivity and σ_{Op} is the optical conductivity. A higher FoM value corresponds to a better agreement between the conductivity and transparency. Figure 2.1 shows the dependence of the performance of several TCEs with respect to amd and FoMs [34].

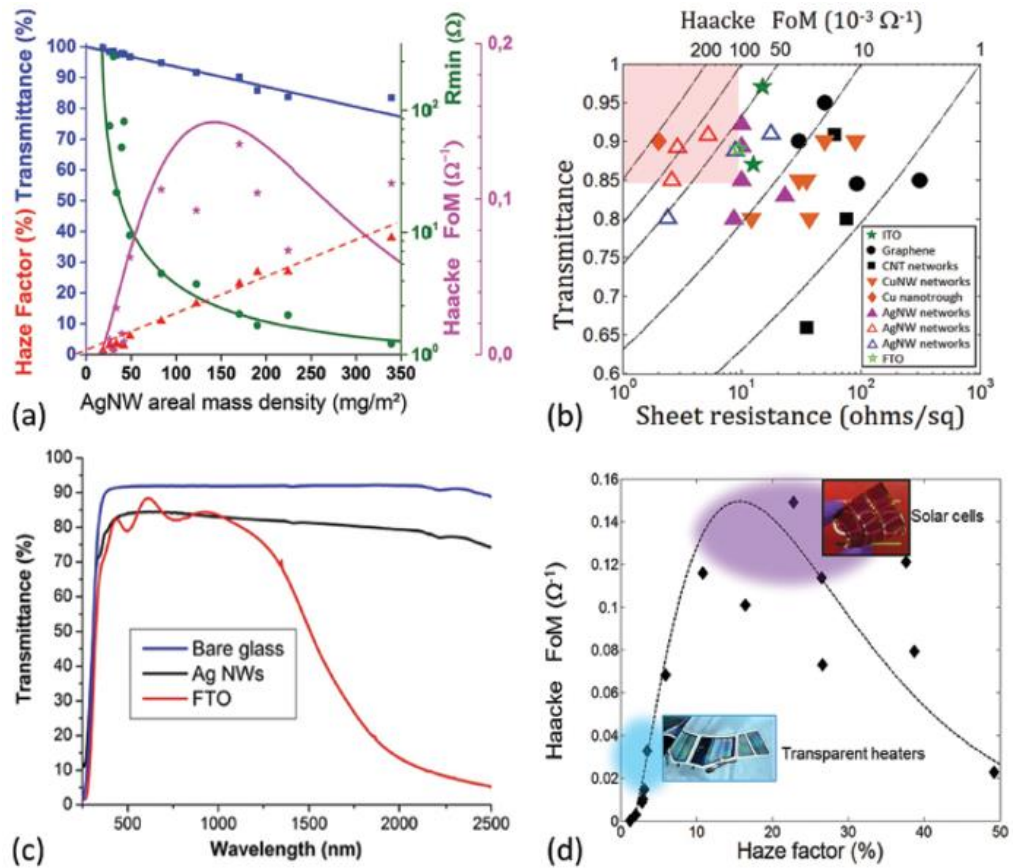


Figure 2. 1 (a) Optical transmittance, haze factor, FoMs, sheet resistance vs areal mass density. (b) Transmittance with respect to sheet resistance for several TCEs including dashed lines showing FoMs. (c) Transmittance comparison of bare glass, Ag NWs and FTO, all of which have the same sheet resistance of $\sim 11 \Omega/\text{sq}$. (d) Dependence of haze factor to FoMs for Ag NW networks [34].

The linear dependence of optical transmittance and power law decrease of sheet resistance with increasing areal mass density can be observed in Figure 2.1 (a). Moreover, FoM curve of Ag NWs shows a peak approximately at 130 mg/m^2 , which indicates the optimum network density of Ag NWs [35]. High optoelectronic performance of metallic nanowires which is also supported by high FoM values can be seen in Figure 2.1 (b). The optical transparency of metallic nanowires is very high

for a broad range of wavelengths including visible and near infrared (NIR) regions. Figure 2.1 (c) shows this behavior by comparing the behavior of Ag NWs with FTO where both of them have the same sheet resistance of $11 \Omega/\text{sq}$ and optical transmittance of 90% at 550 nm [34]. Lastly, Figure 2.1 (d) shows the change in haze with respect to FoM for the Ag NW networks.

2.2. Silver Nanowires

Due to their inherent conductivity and mechanical robustness, Ag NWs were investigated in flexible and stretchable devices. Some of these devices include transparent heaters [36], light emitting devices [4], heatable textiles [37], solar cells [38], touch screens [39] and radio frequency antennas [40].

Several methods were proposed for the synthesis of Ag NWs such as ultraviolet photo reduction [41], solid liquid arc discharge method [42], template guided methods [43], hydrothermal synthesis [44] and polyol method [45], [46]. Among them, polyol method has been considered as the most convenient one for the synthesis of Ag NWs in terms of simplicity, low cost and high yield. Polyol method involves the reduction of metal salts in the presence of a hot polyol with the help of a capping agent. Ethylene glycol (EG) is the most widely used polyol, since it can dissolve both silver nitrate (AgNO_3) and polyvinylpyrrolidone (PVP). PVP acts as a capping agent, which controls the growth rates of Ag nanoparticles as well as prevents their agglomeration. Moreover, chlorine ions are utilized to provide slower reaction kinetics and more stable nanowire formation. Sodium chloride (NaCl) is the most commonly used chlorine ion source in the polyol method.

Accordingly, AgNO_3 salt dissolved in EG and Ag^+ ions are formed. Then, Ag^+ ions are reduced into Ag atoms by EG at elevated temperatures ($\sim 160^\circ\text{C}$). Ag atoms form various types of nanoparticles by homogenous nucleation and the nanoparticles having the multi-twinned particle (MTP) morphology can grow into nanowires in the presence of PVP. PVP molecules attach onto (100) facets on Ag nanoparticles and

leaves (111) facets as active sites for Ag atoms to accumulate on. As Ag atoms accumulate on the (111) facets, the nanowire grows in an anisotropic manner along [110] direction. The Ag NWs produced by polyol method typically have the dimensions of several microns in length and several tens of nanometers in diameter [47]. Figure 2.2 gives the schematic illustration of synthesis process including the formation of a nanorod from an MTP and the addition of Ag atoms to the ends of the nanorod to form a nanowire.

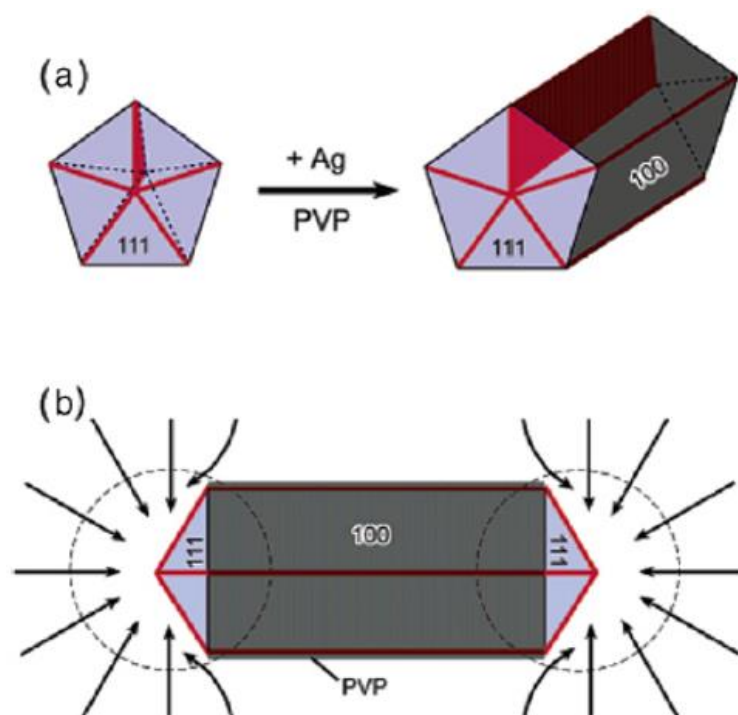


Figure 2. 2 Schematic representation of the synthesis process (a) formation of a nanorod from an MTP. (100) surfaces are confined with PVP and (111) facets left as active sites for Ag atom accumulation. (b) addition of Ag atoms on (111) surfaces (shown by arrows) and anisotropic growth of a nanowire into [110] direction [47].

A detailed parametric study of polyol synthesis of Ag NWs was performed by Coskun et al. in 2011 [46]. The effect of temperature, injection rate, stirring rate, PVP:AgNO₃ ratio and the amount of NaCl on the morphology of Ag NWs were investigated. It was

found that the temperature should be above a certain level to make anisotropic growth favorable. The optimum reaction temperature was defined as 170 °C. Injection rate determines the final morphology of Ag NWs and it was defined as 5 ml/h. If the injection rate is slower or faster than 5 ml/h, micron sized Ag NPs were found to form in addition to Ag NWs. As mentioned above, PVP provides the formation of nanowires by confining certain surfaces of Ag NPs. The optimum molar ratio of PVP:AgNO₃ was determined as 7.5:1 and beyond that value Ag NPs were found to accompany Ag NWs. NaCl was found to play a vital role in the synthesis of Ag NWs. Under slow reaction kinetics, the formation of Ag NWs is favorable. The optimum NaCl amount was decided as 12 μM to obtain Ag NWs without undesired Ag NPs. Lastly, stirring rate was found as 1000 rpm to obtain the desired diameter and length distribution of NWs.

After synthesis, the NW solution consists of both NWs and reaction by-products. By-products include nanoparticles that was not used to grow NWs. Therefore, a purification step is needed to separate NWs from the by-products and organic solution. Generally, the solution is washed with acetone and ethanol for several times and the NWs were dispersed in methanol, ethanol or DI water, depending on the subsequent use.

Random network of Ag NWs can be obtained by spray coating, drop casting, spin coating, rod coating and vacuum filtration. All of these methods utilize the advantage of being solution processable. Among them, spray coating and rod coating provide more homogeneous, uniform and surface scalable films.

As mentioned before, Ag NWs have a surfactant layer (PVP) over their surface. This polymeric layer increases the contact resistance between the nanowires. Thus, a thermal annealing step is required to fuse the junction points and decrease the contact and sheet resistance. Figure 2.3 (b) and (d) show the fusion of Ag NW junctions after annealing at 200 °C for 20 minutes, whereas (a) and (c) show as-deposited Ag NWs.

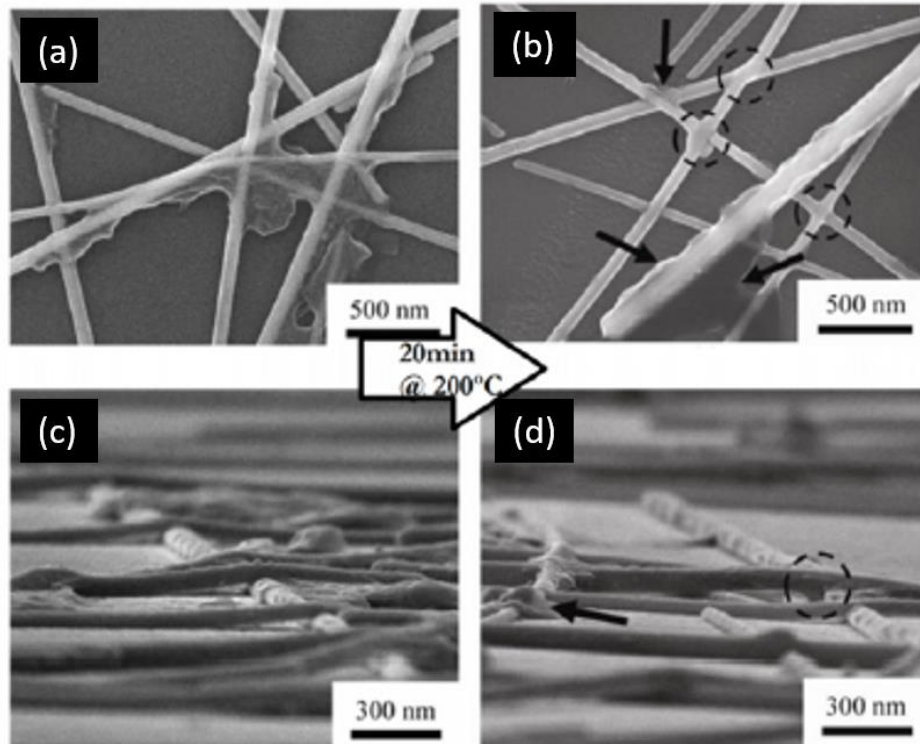


Figure 2. 3 SEM images of as-deposited Ag NW network (a) and (c) and annealed at 200 °C for 20 minutes (b) and (d) [47].

The need for thermal annealing at 200 °C limits the choice of substrates [47]. The polymeric substrates mainly used for flexible devices cannot withstand these elevated annealing temperatures (> 150 °C). Moreover, sensitive layers such as polymeric photoactive layer in OSCs can get damaged if spray coating is performed. Furthermore, roughness of Ag NW networks is another issue that should be solved in order to avoid shorting problems in device applications. Many different techniques were suggested to optimize the roughness of Ag NW networks such as mechanical pressing [48], polymer coating [3] and transfer processes [49]. With transferring methods, it is possible to fabricate Ag NW thin films on different substrates and transfer the final structure directly onto the device. Thus, the receiver surface can be preserved from the detrimental processing conditions of Ag NW networks. As a result,

transfer processes become prominent solutions against these two major drawbacks of Ag NW networks.

Madaria et al., performed the dry transfer of Ag NW networks using PDMS stamps [49]. Ag NW network is formed on an anodic aluminum oxide (AAO) membrane by vacuum filtration and transferred onto a PDMS stamp by applying pressure on AAO membrane. Ag NW network is removed completely from the membrane surface and collected on PDMS. Then, PDMS stamp bearing Ag NW network is pressed onto the receiver substrate and PDMS is peeled off from the surface after a few minutes. Figure 2.4 summarizes all steps of transfer process together with corresponding SEM images of the receiver substrates.

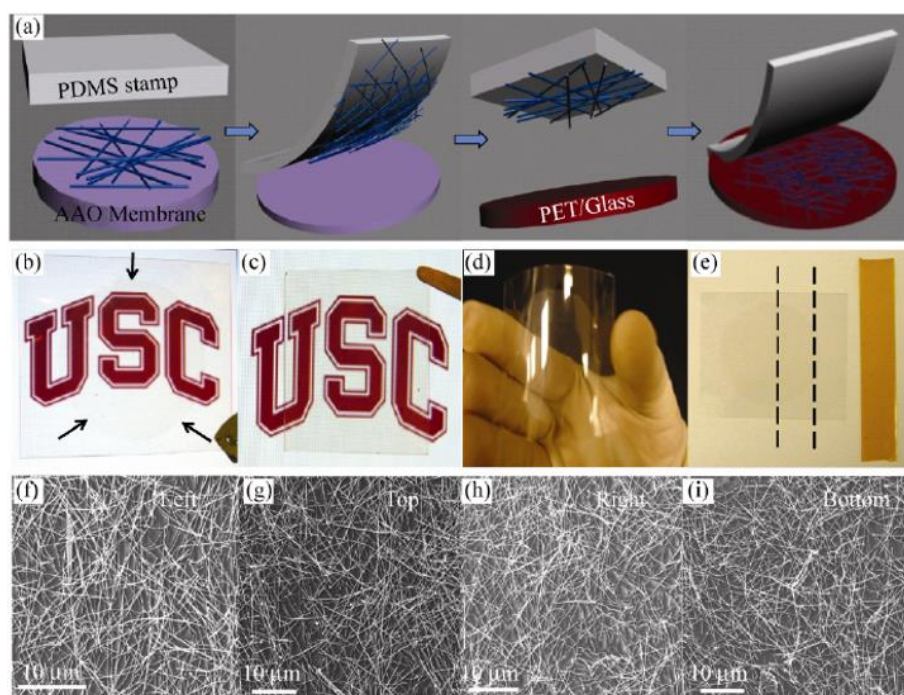


Figure 2. 4 (a) Schematics of PDMS transfer process, (b) Transferred Ag NW network on PET substrate, (c) Transferred Ag NW network on glass substrate, (d) The flexibility of the film on PET, (e) Adhesion test results of transferred Ag NW film, tape is peeled from the region between the dotted lines and Ag NWs still remain on the surface, (f) to (i) SEM images of top, left, bottom and top of the transferred film showing the uniformity, respectively [49].

Madaria et al., also demonstrated that Ag NW network can be annealed on AAO membranes and then transferred to the receiver substrates [49]. Two data sets of comparable samples (annealed and as-received) are prepared and their optoelectronic performance is compared. The annealed samples have 85% transparency and 10 Ω /sq of sheet resistance, whereas as-received samples have 85% transparency at 30 Ω /sq sheet resistance. Figure 2.5 shows the comparison of optoelectronic performance of annealed and as-received samples and the SEM image of a fused junction following annealing.

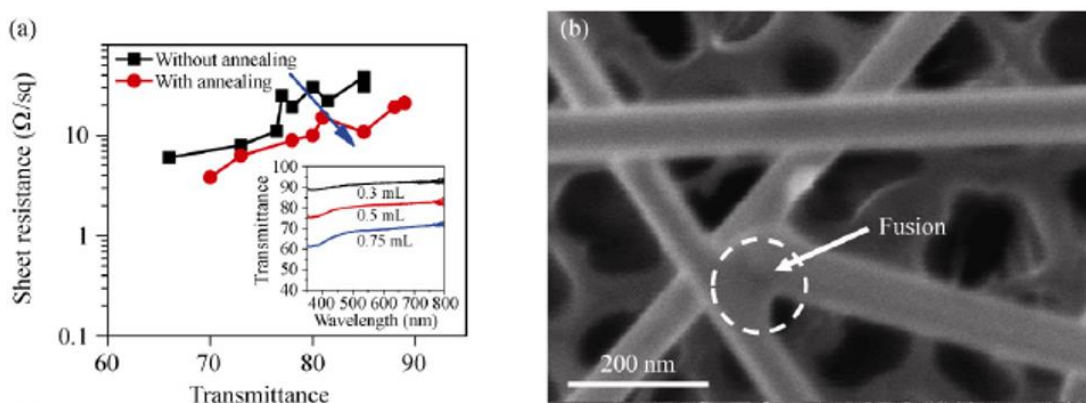


Figure 2. 5 (a) Sheet resistance vs transmittance curves of annealed and as-received samples. (b) SEM image showing fusion of a junction [49].

PDMS stamp can be patterned by optical lithography and patterned Ag NW network can be obtained simply by spraying onto the patterned PDMS substrate. Madaria et al., proved this method to obtain pixelated Ag NW thin films [50]. After spraying Ag NWs onto PDMS stamp, the receiver substrate is placed onto a hot plate at 120 °C and PDMS stamp bearing the Ag NWs is pressed against the substrate for several minutes. Following this step, PDMS stamp is peeled off from the surface and the patterned nanowire film is transferred to the substrate as illustrated in Figure 2.6. Corresponding (a) and (b) photo and SEM image of the patterned Ag NW film is shown in Figures 2.6 (c) and (d), respectively.

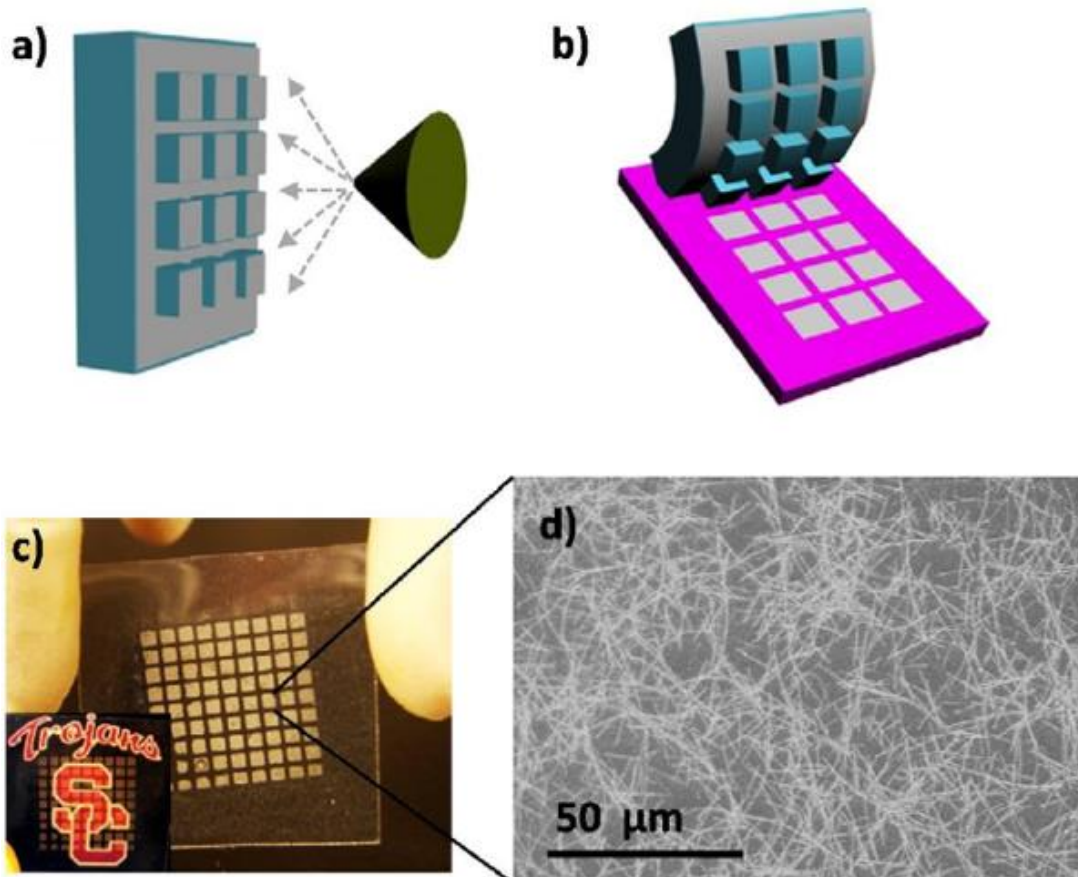


Figure 2. 6 Schematics showing (a) Spray coating on a patterned PDMS stamp, (b) Transfer of pixelated Ag NW thin film on a receiver substrate, (c) Photo of the patterned sample and (d) SEM image of Ag NW thin film obtained from a pixel [50].

Gaynor et al., reported an RMS roughness value for Ag NWs embedded in PEDOT:PSS much lower than that of bare Ag NW film [3]. They fabricated Ag NW/PEDOT:PSS composite TCEs which have far better optoelectronic properties compared to ITO and used it as a front electrode of OSC, based on P3HT:PCBM. For this purpose, Ag NWs were drop casted onto a glass substrate followed by lamination over PEDOT:PSS layer. As the thickness of PEDOT:PSS increased, the flatness of the composite film was found to increase. AFM results showed an RMS roughness of 11.9 nm, where nanowires can be 20-30 nm above the film surface. As compared with bare

Ag NW networks of which peak to peak roughness value can reach about 200 to 300 nm, embedding Ag NW network into a polymer significantly reduces the roughness. The top, tilted and side-view SEM images and an AFM image of the composite electrodes are given in Figure 2.7.

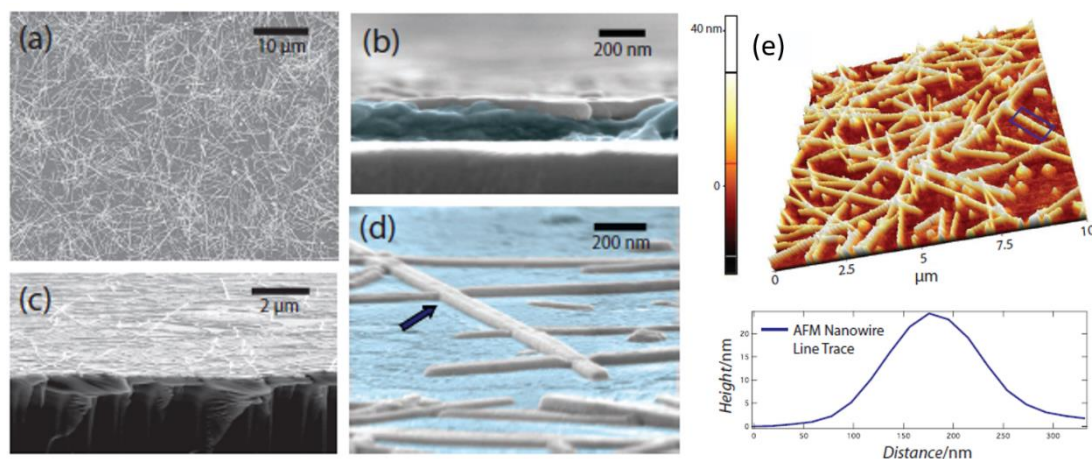


Figure 2. 7 SEM images of composite electrode (a) top view, (b) cross-sectional view, (c) Angled cross-sectional view, (d) Angled cross-sectional view at a higher magnification, (e) AFM image of composite electrode surface and height profile of a nanowire. The nanowire used for height profile is marked with a blue box on AFM image [3].

2.3. Experimental Details

All glassware used in the process were cleaned using Alconox detergent and deionized water followed by sonication in acetone (99.8%), isopropyl alcohol (99.8%) and deionized water (18.3 M Ω) for 20 minutes, each. All chemicals used in the experiments were purchased from Sigma – Aldrich and used without further purification.

2.3.1. Synthesis of Silver Nanowires

In the synthesis of silver nanowires, the large-scale polyol process was followed, which was modified from Coskun et al. [46]. Accordingly, 80 ml and 0.45 M EG solution with PVP (MW=55000) was prepared and 1 mM NaCl (99.5%) was added to the solution. The solution was heated to 100 °C and stirred at 1000 rpm with a magnetic stirrer at the same time, in order to dissolve PVP and NaCl in EG. After complete dissolution, the solution was cooled to room temperature. Meanwhile, a 40 ml EG solution of 0.12 M AgNO₃ (99.5%) was prepared by stirring on a hot plate without heating. After complete dissolution, the EG solution of AgNO₃ was placed in an oil bath, which was at 120 °C. After that, the EG solution with PVP and NaCl was added to AgNO₃ solution dropwise. When the addition was finished, the temperature of oil bath was raised to 160 °C. Once the temperature of the solution reached 160 °C, the solution was kept at that temperature for 90 minutes while stirred at 1000 rpm with a magnetic stirrer.

Following synthesis, the nanowires are in a solution with excess solvent, excess PVP and by-product nanoparticles. In order to separate nanowires from the rest of the solution, a centrifugation process is needed. First, the solution is washed in acetone and centrifuged at 7000 rpm for 10 minutes. After that, the solution is washed in ethanol and centrifuged at 7000 rpm for 10 minutes. Then, the nanowires are dispersed in ethanol for further processing (Figure 2.8 (a)).

2.3.2. Fabrication of Ag NW/PDMS Electrodes

Glass substrates with dimensions of 2.54 cm × 2.45 cm are cleaned in acetone, isopropanol and distilled water using an ultrasonic bath. Then, they are dried under nitrogen gas flow. Ag NW network is formed using spray deposition technique. For this, the glass substrates are placed on a hot plate using a heat-resistant tape and the temperature of the hot plate is set to 120 °C. Ag NWs are sprayed onto the glasses using an air brush as shown in Figure 2.8 (b).

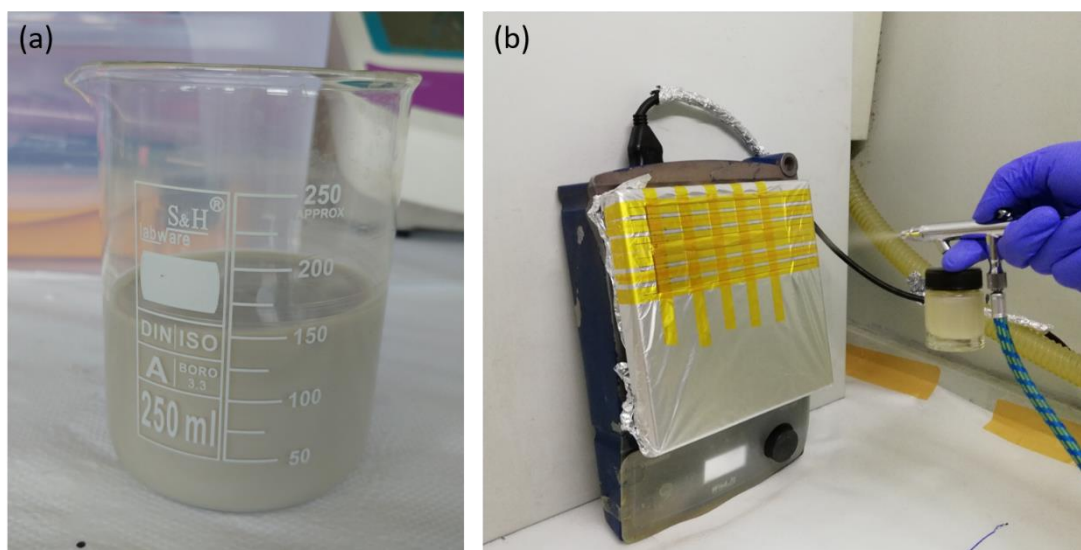


Figure 2. 8 Photographs of (a) Ag NWs dispersed in ethanol and (b) spray deposition of Ag NWs onto glass substrates via airbrush.

In order to obtain a uniform network, the pressure of air brush is adjusted to 2 atm and the distance between the air brush nozzle and hot plate is fixed to 10 cm. Subsequent spray cycles determines the density of the Ag NWs. There should be a percolation between Ag NWs to obtain electrical conductivity.

PDMS is prepared by mixing a silicon elastomer (Sylgard 184) and its curing agent. They are mixed with a ratio of 12:1 and stirred for 5 minutes. Then, the mixture is placed in a vacuum furnace for 30 minutes of degassing. Afterwards, spin coating of PDMS on Ag NW electrodes is performed at 500 rpm for 40 seconds. Coated samples are cured at 160 °C for 20 minutes. In order to lift Ag NW/PDMS electrodes from the glass substrates, the samples are immersed in hot water at 60 °C for 30 seconds. Then, Ag NW/PDMS electrodes can be simply lifted with the help of a tweezer.

2.4. Characterization Methods

2.4.1. SEM Analysis

SEM analyses of transparent and conducting Ag NW/PDMS electrodes are carried out by FE-SEM (Nova NanoSEM 430) operated at a voltage of 10 kV. Samples are prepared by peeling the Ag NW/PDMS layer off the glass and then placing on the SEM holder via carbon tape. An additional 5 nm thick conductive gold layer is deposited on top of the Ag NW/PDMS samples. Gold deposition is performed with an operating voltage and current of 1.5 kV and 10 mA for 1 minutes, respectively. No additional conductive layer is used for bare Ag NW samples.

2.4.2. Transparency Measurements

UV-Vis characterization of Ag NW/PDMS electrodes is carried out with Bentham PVE300 photovoltaic characterization system between the wavelength range of 400-1000 nm. Bare PDMS substrates were utilized for baseline correction.

2.4.3. Sheet Resistance Measurements

Four-point probe measurements of Ag NW/PDMS samples are carried out by Signatone Pro4-440 N system to determine sheet resistance values with the unit of Ω/sq .

2.4.4. AFM Measurements

Topography of Ag NW/PDMS samples are analyzed by AFM (Veeco MultiMode V). Measurements are performed in tapping mode for an area of $10\ \mu\text{m} \times 10\ \mu\text{m}$.

2.5. Results

Ag NWs are purified following the synthesis process. The top-view SEM image in Figure 2.9 shows purified Ag NWs. As can be seen from the SEM image, no by-product particles such as nanoparticles, multi-twin particles are observed.

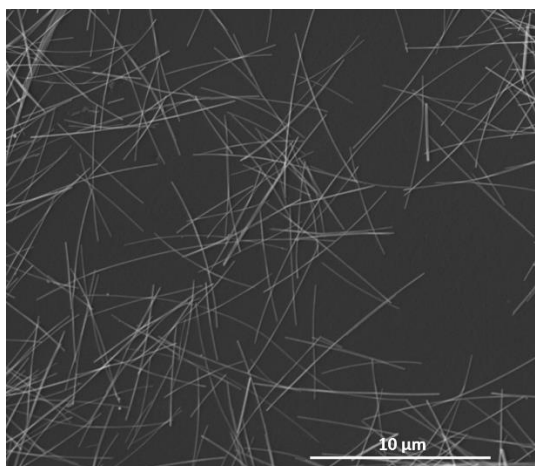


Figure 2. 9 SEM image of purified Ag NWs.

The length and diameter distribution of Ag NWs utilized in this work is obtained from the SEM images. 100 NWs are used for this purpose. The average diameter and length of Ag NWs is then calculated as 60 nm and 8 μm, respectively. The distribution graphs are provided in Figure 2.10 (a) and (b), respectively.

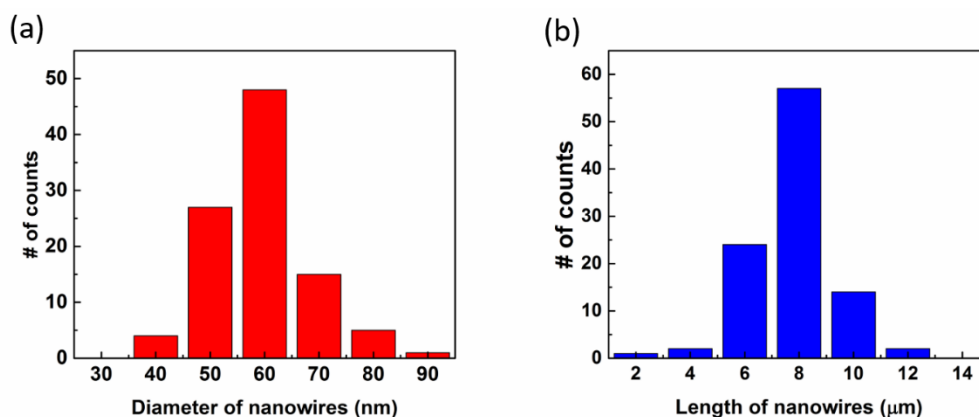


Figure 2. 10 (a) Diameter and (b) length distribution of Ag NWs used in this work.

Ag NWs embedded in PDMS films is peeled off from the glass substrate to transfer Ag NWs onto the PDMS surface. This glass substrate is investigated via SEM to determine the effectiveness of the PDMS-assisted transfer method. It is found from

the SEM images that, approximately 100% of Ag NW network is transferred to the PDMS surface. SEM images in Figure 2.11 reveals that there are almost no NWs and a network structure on the glass substrate. Moreover, excessive gold coating had to be performed to carry out this analysis. Apparent spheres on the glass substrates as evident from the SEM images are gold nanoparticles and not related with the PDMS-assisted transfer procedure.

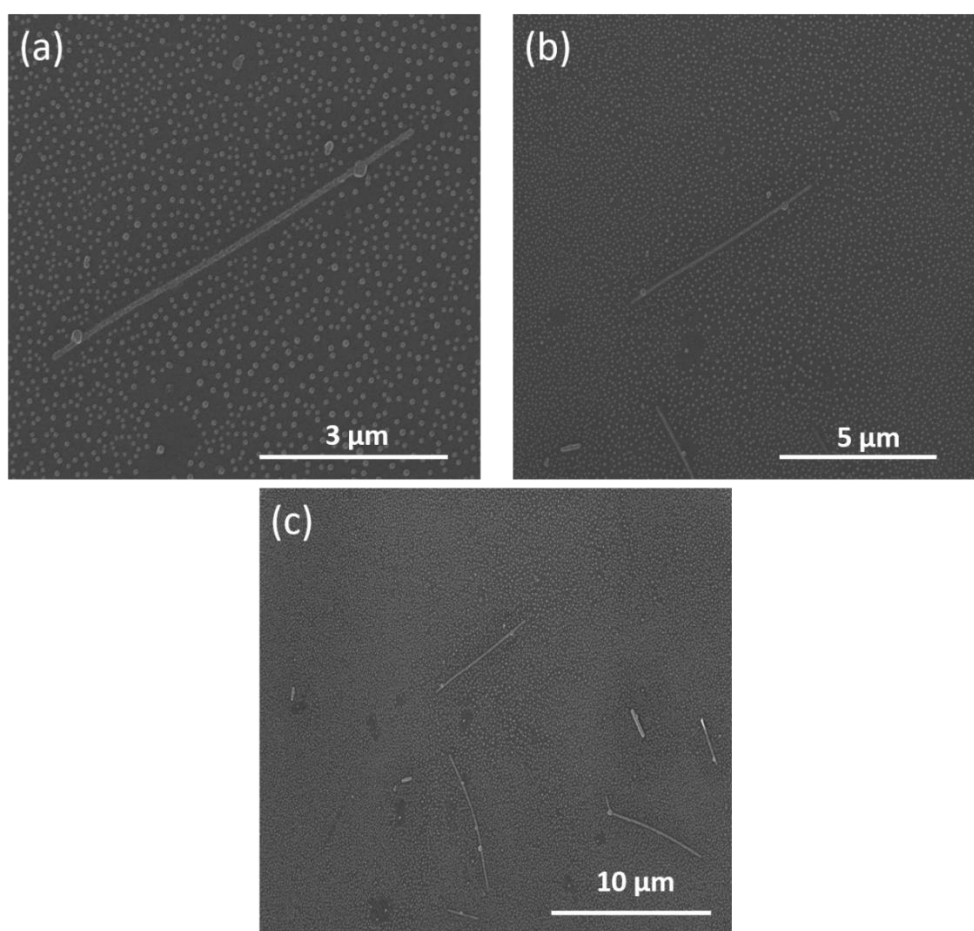


Figure 2. 11 Different magnification SEM images of glass substrate after transfer of Ag NW network at magnifications of (a) 40000X, (b) 20000X and (c) 10000X.

According to optical measurements the transmittance of bare PDMS substrate is found as 96% at a wavelength of 550 nm. Then, transmittance of Ag NW/PDMS samples is measured and bare PDMS is used for the baseline corrections for obtaining

transmittance of Ag NW network. Transmittance curves of bare PDMS and Ag NW/PDMS electrodes with sheet resistances of 10, 25 and 50 Ω/sq are shown in Figure 2.12.

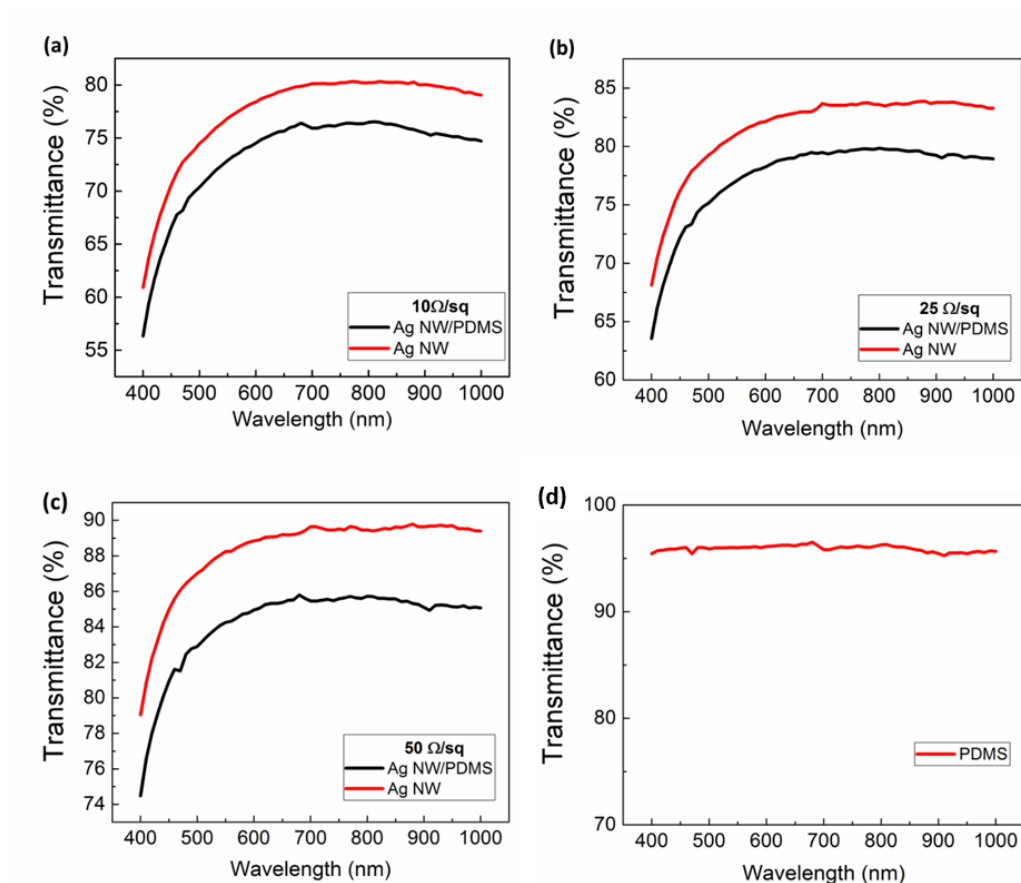


Figure 2. 12 Transmittance curves of Ag NW and Ag NW/PDMS electrodes with sheet resistances of (a) 10, (b) 25 and (c) 50 Ω/sq , (d). Transmittance curve for bare PDMS.

Coating PDMS over Ag NW networks results in a decrease of 4% in transmittance. Moreover, decreased sheet resistance reduces the transmittance of Ag NW networks. As can be seen from Figures 2.13 and 2.14, transmittance of Ag NW networks can be simply tuned by controlling the NW density during spray coating. This is due to increasing nanowire density which decreases the passage of light through the network.

FoMs for Ag NW networks and Ag NW/PDMS thin films are calculated according to Haacke's formula [33] to compare with that for ITO and FTO. The results are provided in Table 2.1.

Table 2. 1 FoMs of Ag NW, Ag NW/PDMS, ITO and FTO thin films

Material	Sheet Resistance (Ω/sq)	Transmittance at 550 nm (%)	Haacke's FoMs ($10^{-3} \Omega^{-1}$)
Ag NW	10	76.9	7.23
Ag NW/PDMS	10	72.9	4.24
Ag NW	25	81.1	4.92
Ag NW/PDMS	25	77.1	2.97
Ag NW	50	88.2	5.70
Ag NW/PDMS	50	84.2	3.58
ITO [51]	12	88.1	23.50
ITO [52]	25	80.0	4.29
ITO [53]	52	83.0	2.98
FTO [54]	11	85.0	17.99
FTO [54]	24	86.1	9.37
FTO [54]	41	84.5	4.52

FoMs of Ag NW/PDMS thin films is lower than that of Ag NW networks due to their lower optical transmittance. Moreover, FoMs of Ag NW networks and Ag NW/PDMS thin films is lower than that of ITO and FTO for lower sheet resistance values, since the difference between optical transmittances become more remarkable for lower sheet resistance values. However, as sheet resistance values increase, FoM of Ag NW networks becomes equal or higher than those of ITO. Yet, FoMs of FTO is superior to those of both Ag NW and Ag NW/PDMS. Since FoMs emphasize the significance of optical transmittance, they can be increased by improving optical transmittance of Ag NW networks.

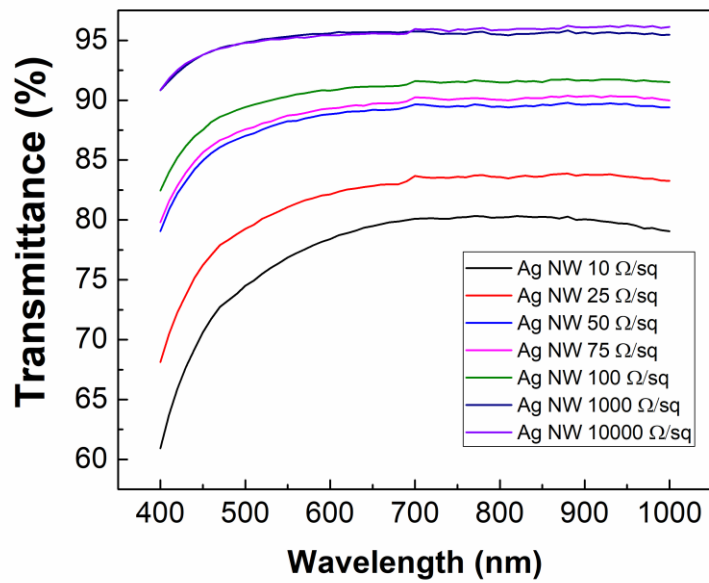


Figure 2. 13 Transmittance curves for Ag NW network with different sheet resistances

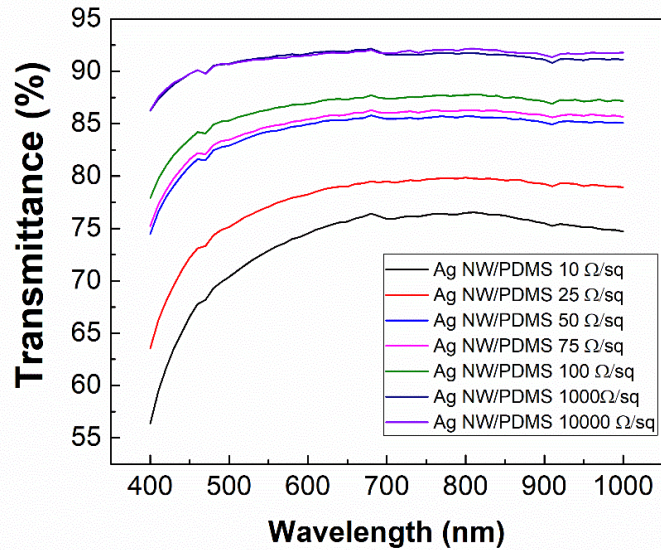


Figure 2. 14 Transmittance curves for Ag NW/PDMS with different sheet resistances

High surface roughness of as-deposited nanowire networks causes shorts when utilized in thin film devices like OSCs. Therefore, roughness should be decreased for obtaining high performance devices. RMS roughness of Ag NW/PDMS electrodes are obtained as 29 nm, whereas as-deposited Ag NW network has an RMS roughness of 54 nm [4]. AFM phase and 3D images of Ag NW/PDMS electrodes and bare PDMS are given in Figure 2.15. RMS roughness of bare PDMS sample was obtained as 1.24 nm. Accordingly, coating PDMS over Ag NW networks decreases RMS roughness value by filling the voids between nanowires.

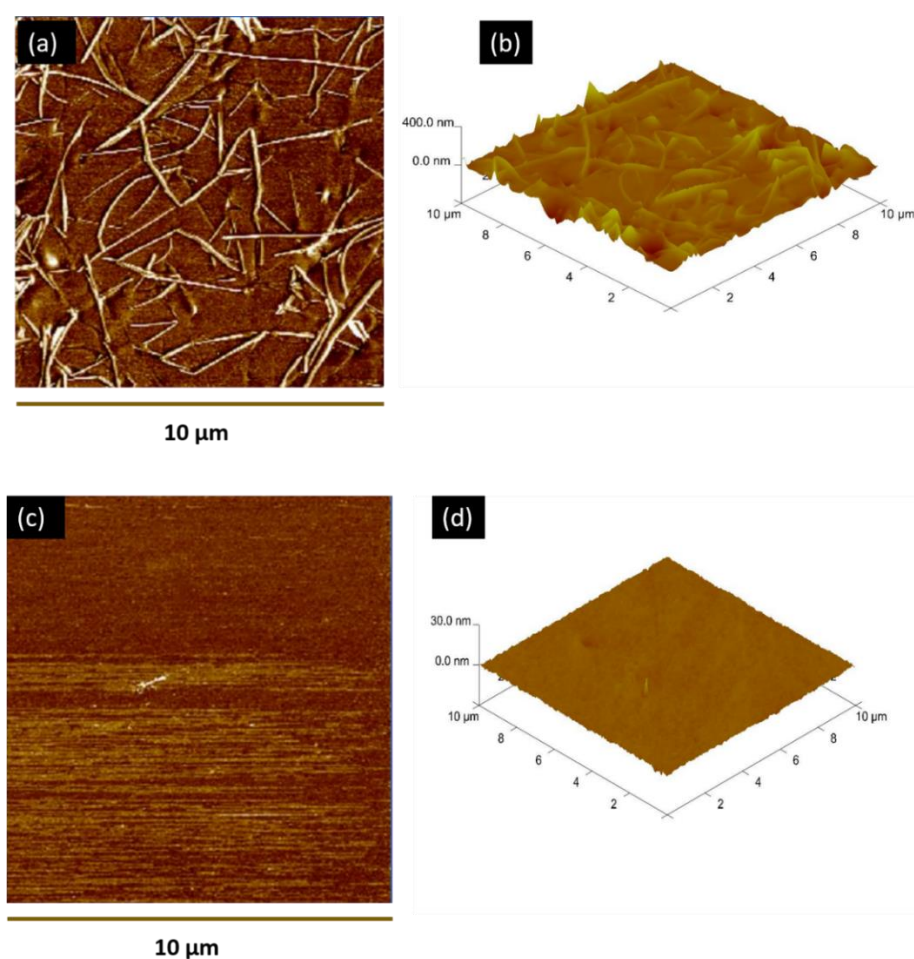


Figure 2. 15 AFM images of Ag NW/PDMS electrodes showing (a) phase image, (b) 3D image and bare PDMS showing (c) phase image and (d) 3D image, respectively.

CHAPTER 3

TRANSPARENT AND CONDUCTING Ag NW/PDMS ELECTRODES FOR ORGANIC SOLAR CELLS

3.1. Introduction

The energy coming from the sun in an hour is more than the energy that mankind can utilize in one year [55]. According to ASTM standard for the AM1.5G spectrum, 1000 W/m² solar irradiance is observed on the surface of the Earth on a cloudless day [56]. Therefore, solar energy has the highest potential among other renewable energy sources for fulfilling the increasing energy demand of the mankind. Solar cells absorb the solar radiation and directly convert it to electricity. The very first devices achieving this conversion are inorganic solar cells having p-n junctions in their structure. Although these first-generation solar cells can yield quite high-power conversion efficiencies (PCEs), the research has continued and resulted with second- generation or thin film solar cells such as amorphous silicon, cadmium telluride (CdTe), gallium arsenide (GaAs) and copper indium-gallium diselenide (CIGS). More recently, third-generation novel solar cells have emerged, which contain OSCs as a subset. OSC holds the benefits of low cost, mechanically flexibility and solution-processability.

3.2. Device Architecture and Operation Principles

Typical device architecture of OSCs consists of a photoactive layer sandwiched between two electrodes. One of the electrodes should be transparent to incident light for maximizing the absorption of solar irradiation and commonly made of ITO thin films deposited on glass or polyethylene terephthalate (PET) substrates. The photoactive layer typically consists of polymeric donor and acceptor materials. Most commonly fullerenes are used as acceptor materials. The photoactive layer can be a single layer, where a single layer of donor and a single layer of acceptor are stacked,

a double layer where two single layers are stacked or a bulk heterojunction (BHJ) where donor and acceptor materials are blended. In BHJs, the blending of donor and acceptor material decreases the average distance that the carriers travel and thus charge carriers can be collected more efficiently [57], [58]. This in turn, improves the efficiency of the solar cells.

There are two different device architectures, which are called as normal geometry and inverted geometry. In normal geometry, typically ITO is used as the anode and coated with a hole transporting layer (HTL). PEDOT:PSS is the most commonly used HTL material to enhance the charge collection. Moreover, various transition metal oxides have also been adopted as HTL like nickel oxide (NiO) [59], molybdenum oxide (MoO_3) [60] and vanadium oxide (V_2O_5) [61]. Above HTL, organic active layer is deposited. Lastly, low work function metals such as Al is used as the cathode. This architecture has some drawbacks. Firstly, the cathode material is evaporated on the photoactive layer using vacuum processes and this reduces the operational lifetime [62]. Secondly, the acidic nature of PEDOT:PSS solution would etch the underlying ITO layer and result in the corrosion of ITO in long term [63]. Lastly, the low work function metals used as cathode are prone to oxidation [64]. At this point, inverted solar cells become prominent. In this structure, ITO is used as the cathode and a high work function metal is used as the anode. It should be noticed that ITO should be modified in order to be utilized as a cathode. For efficient electron extraction, titanium oxide (TiO_x) [65] or zinc oxide (ZnO) [66] can be coated on top of ITO. In addition, the interface between the anode and photoactive material should be enhanced by the employment of a layer like PEDOT:PSS to increase the charge collection efficiency [67]. The structures of these two geometries and the positions of the layers are schematically shown in Figure 3.1. The corresponding functions of these layers are summarized in Table 3.1.

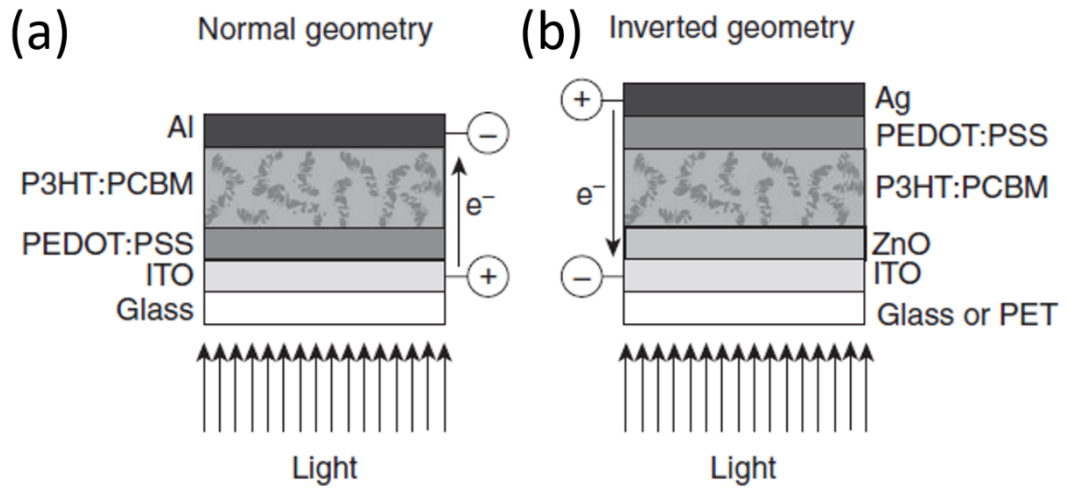


Figure 3. 1 BHJ OSC devices with (a) normal geometry and (b) inverted geometry [62].

Table 3. 1 Materials used in normal and inverted geometries and their roles [62].

Normal geometry					
Substrate	Anode	Hole transport layer	Active layer	Electron transport layer	Cathode
Glass PET	ITO	PEDOT:PSS MoO ₃ V ₂ O ₅	P3HT:PCBM	TiO _x ZnO	LiF / Al LiF / Au
Inverted geometry					
Substrate	Cathode	Electron transport layer	Active layer	Hole transport layer	Anode
Glass PET PEN	ITO Ag-solid Al/Cr	ZnO TiO _x Cs ₂ CO ₃	P3HT:PCBM	PEDOT:PSS	Ag Ag-grid

PET = polyethylene terephthalate; PEN = polyethylene naphthalate; ITO = indium tin oxide;
 PEDOT:PSS = poly(3,4-ethylenedioxythiophene):poly(styrenesulfonate); MoO₃ = molybdenum trioxide; V₂O₅ = vanadium pentoxide;
 P3HT = poly(3-hexylthiophene); PCBM = [6,6]-phenyl C61 butyric acid methyl ester (fullerene derivate);
 TiO_x = titanium oxide; ZnO = zinc oxide; LiF = lithium fluoride; Cs₂CO₃ = cesium carbonate;
 Al = aluminum; Au = gold; Ag = silver; Cr = chromium.

Each donor and acceptor material possess a highest occupied molecular orbital (HOMO) and a lowest unoccupied molecular orbital (LUMO) level. Figure 3.2 represents a donor acceptor interface schematically. The energy difference between HOMO and LUMO levels create the bandgap of the polymer. The energy difference between the HOMO of donor and LUMO of acceptor defines open circuit voltage (V_{oc}) of the BHJ OSC.

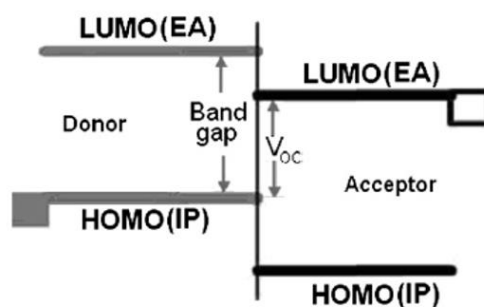


Figure 3. 2 Energy diagram of donor acceptor interface [68].

An exciton (a bound electron-hole pair) is generated upon absorption of a photon in OSCs. Operation principles of OSCs can be explained through the following four steps [69].

1. Absorption of Photons and Exciton Generation: As the incident sunlight is absorbed by the photoactive material, it excites the electron (also called as negative charge carrier) to the LUMO. Simultaneously, a hole remains in the HOMO which is a positively charged carrier. As a result, an electron-hole pair is generated, which is Coulombically attracted. This electron-hole pair is called as an exciton.

The incident light should be absorbed at a maximum level by the photoactive layer to obtain high efficiencies in OSCs. Generally, donor part of a BHJ OSC absorbs the light. As compared to inorganic solar cells, OSCs can absorb the light efficiently with lower photoactive layer thicknesses (up to 100 nm) due to high absorption coefficients (10^7 m^{-1}) of donor materials [69]. In addition, the thickness of photoactive layer should

be confined to 100-150 nm due to its weak charge carrier mobility. The absorption of light can be improved by utilizing low bandgap donor materials, which enhances the PCE of device, consequently [70]. For instance, a 1.1 eV bandgap material can absorb 77% of AM1.5 photon flux, whereas a 1.9 eV bandgap material can absorb only 30% of it [68].

2. *Exciton Diffusion:* The diffusion of generated exciton takes place through the donor phase. The exciton eventually reaches to the donor-acceptor interface. If the distance between the generated exciton and the donor-acceptor interface is greater than exciton diffusion distance (10-15 nm), recombination of charge carriers can be observed. BHJ concept was developed to reduce the distance between donor-acceptor interfaces, which reduces the distance to be travelled by excitons and recombination rate as a consequence [71]. Thus, the thickness of the photoactive layer plays an important role in charge generation.

3. *Exciton Dissociation:* When the exciton reaches a donor-acceptor interface, it separates into a free electron and a hole. The donor and acceptor materials have different LUMO and HOMO values. This difference causes the formation of electrostatic forces in the donor-acceptor interface. Charge carriers are separated by the internal electric field and delivered through the respective donor and acceptor materials.

4. *Transport and Collection of Free Charge Carriers:* Dissociated charge carriers are transported through the device. Then, the electrons are collected at the cathode, whereas the holes are collected at the anode. The work function differences between the two electrodes of the device causes an internal electric field which drives the free charge carriers to the respective electrodes. Mobility and thickness of the photoactive materials have the most important roles in transportation and collection of free charge carriers. As the material gets thicker, the probability of charge carrier recombination grows. Moreover, the interfacial mismatch between the layers should be minimized to avoid loss of generated carriers. The work function of anode should be matching with

the HOMO of the donor whereas, the work function of cathode should be matching with the LUMO of the acceptor [72]. Furthermore, ohmic contacts should be ensured to minimize power losses for both electrodes during charge collection.

The flowchart of photocurrent generation including these 4 steps is illustrated in Figure 3.3 (a) and (b) in terms of band level and donor-acceptor interface, respectively.

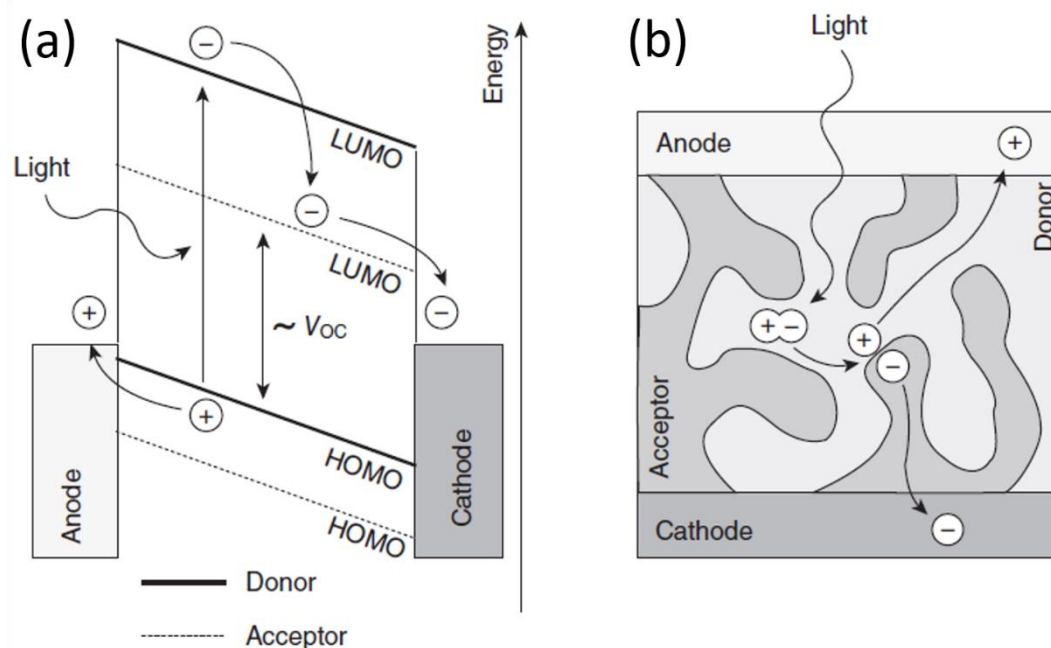


Figure 3. 3 (a) Schematic representation of photocurrent generation in terms of photon absorption, exciton generation, exciton dissociation and charge carrier collection, (b) schematic diagram of charge carrier transportation in photoactive material of a BHJ device [62].

Mostly, three parameters play a significant role in the operation of solar cells. These are short circuit current (J_{sc}), open circuit voltage (V_{oc}) and fill factor (FF). Generally, the demonstration of the operational performance and parameters of a solar cell are represented by current density-voltage (J-V) curves. A typical J-V curve showing all these parameters is given in Figure 3.4.

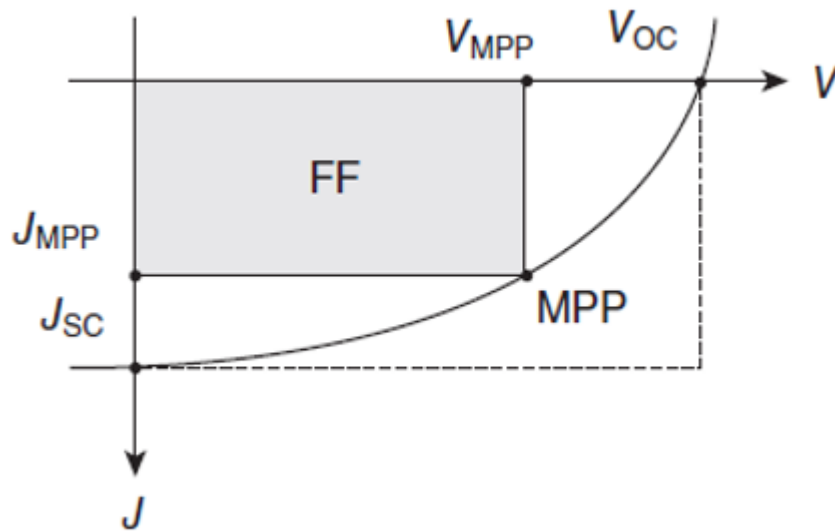


Figure 3. 4 Typical J-V curve of an OSC [62].

Short Circuit Current Density (J_{SC}): When V_{OC} is equal to zero, the maximum amount of photocurrent density is obtained, which is called as J_{SC} . It represents the maximum amount of charge carriers that are generated and collected at the electrodes when no voltage is applied.

Open Circuit Voltage (V_{OC}): It is the voltage, which is not connected to any load in a circuit. In other words, V_{OC} is the difference of electrical potential between two terminals of a device when disconnected from a circuit. V_{OC} of a BHJ OSC is defined as the energy difference between the HOMO of the donor and the LUMO of the acceptor [73].

Fill Factor (FF): Proportion of the maximum output power and product of V_{OC} and J_{SC} is called as FF and determines the maximum power that can be obtained from a solar cell. The shape of the J-V curve describes the FF. The more rectangular the J-V curve, the higher the FF. FF of OSCs are expected to be in the range of 60-65% for a good performance. It is highly affected by variances in the series resistance (R_S) and the shunt resistance (R_{Sh}). R_S represents a collective resistance, which based on the

resistance of all the layers or interfaces and the conductivity of the layers of the cell including the electrodes. High R_S is detrimental for FF, it can even cause short circuit. R_{Sh} is the resistance due to the manufacturing defects. It should be high in order to avoid formation of an alternative path to the photogenerated current. The losses to the shunt therefore should be minimized for an efficient OSC.

These three parameters are expressed in combination to define photovoltaic conversion efficiency (PCE), which is denoted as η . PCE can be defined as the ratio of the maximum electrical power generated by the cell and the power of the incident light with respect to given area. These expressions are given in Equation 1 and Equation 2 below,

$$\eta = \frac{P_{out}}{P_{in}} = \frac{FF (V_{OC} \times J_{SC})}{P_{in}} \quad \text{Eq (1)}$$

$$FF = \frac{V_{MPP} \times I_{MPP}}{V_{OC} \times J_{SC}} \quad \text{Eq (2)}$$

, where, V_{MPP} and I_{MPP} are the voltage and current density at the maximum output power (P_{out}). Generally, the demonstration of the operational performance and parameters of a solar cell are represented by current density-voltage (J-V) curves. A typical J-V curve showing all the aforementioned parameters is given in Figure 3.4.

3.3. Silver Nanowire Networks as Transparent Conducting Electrodes for Organic Solar Cells

ITO is the most commonly used TCE material in OSC devices. However, due to its aforementioned drawbacks, there are many studies to replace ITO with alternative TCE materials.

Song et. al fabricated inverted organic cell (IOSC) devices with Ag NW and ITO bottom electrodes and compared their performances [74]. Ag NW solutions and ITO were coated both on glass substrates and polyether sulfone (PES) substrates. Four

different device architectures are obtained with Ag NW on glass, Ag NW on PES, ITO on glass, ITO on PES substrates and Ag metal was evaporated as the top electrode. ZnO was used as electron selective layer while PEDOT:PSS was used as hole selective layer. The photoactive layer was consisting of P3HT:PC₆₁BM blend. ZnO acted as a buffer layer on top of Ag NW electrodes, which reduces both the roughness of Ag NW network and the possibility of shorting. Ag NW/glass and Ag NW on PES electrodes have showed PCE values of 3.25% and 2.96%, respectively. On the other hand, ITO/glass and ITO/PES electrodes have showed PCE values of 3.46% and 3.05%, respectively. Moreover, Ag NW networks had a $R_{Sh} \sim 16 \Omega/sq$ and a transmittance of 95% at 550 nm. These results have shown that Ag NW networks can be a potential candidate to replace ITO in OSCs.

Gaynor et. al, fabricated fully solution-processed BHJ IOSCs on opaque bottom electrodes [11]. The device architecture was Ag/Cs₂CO₃/P3HT:PC₆₁BM/PEDOT:PSS/Ag NW. Ag NWs were spray coated onto glass substrates and then laminated on top of the PEDOT:PSS layer. After lamination, glass substrate was removed and Ag NW network was transferred over the device in this manner. Ag NW network has established good mating surfaces with PEDOT:PSS and formed a good conductive layer. The fabricated IOSCs has shown a PCE of 2.5% under 100 mW/cm² AM1.5G illumination.

An IOSC device consisting of ITO bottom electrode and poly(2,6-(4,8-bis(5-ethylhexylthienyl) benzo- [1,2-b;3,4-b] dithiophene-alt-5-dibutyl-octyl-3,6-bis (5-bromothiophen-2-yl)pyrrolo[3,4-c]pyrrole-1,4-dione) (PBDTT-DPP) and PC₆₁BM blend as photoactive layer was investigated by Chen et. al [10]. They utilized PEDOT:PSS as anode modification layer and TiO₂ as cathode modification layer. A 20 nm thick TiO₂ layer served as both a protective layer on top of the photoactive layer and also reduces the energy barrier between the top electrode and photoactive layer. Moreover, it improved the adhesion of Ag NW networks. ITO nanoparticles (NPs) were then used to fill the voids between the Ag NWs within the network. After coated with ITO and modified by TiO₂ layer, Ag NW composite electrodes have an average

87% transmission in the wavelength range of 400-1000 nm with a sheet resistance of 30 Ω /sq. Accordingly, the device had an average 61% transmittance over the wavelength range of 400-1000 nm and a PCE of 4%. The J_{SC} value of 12.60 mA/cm² was comparable to the control device with a TiO₂/Al top electrode with a J_{SC} of 13.0 mA/cm².

Chalh et. al, investigated the performance of a tri-layer electrode consisting of ZnO NPs/Ag NW/ZnO NPs (ZAZ electrode) [75]. The integration of ZnO NPs to the electrode structure provides both good adhesion and an improved conductivity by filling the voids between the Ag NWs. Moreover, ZnO NPs prevents the shorting of the device by reducing the root mean square roughness of Ag NW networks from 19 nm to 13 nm. By varying the thickness of the ZnO layers, the electrical and optical properties of the electrodes can be tuned. Accordingly, the best performance was obtained from 13 nm thick ZnO layered stacks with a sheet resistance transmittance of 13 Ω /sq and 88%, respectively. P3HT:PC₆₁BM blend was coated onto both glass/ZnO/Ag NW/ZnO electrodes and glass/ITO/ZnO electrodes. PEDOT:PSS was spun on photoactive layer and Ag metal was evaporated as top electrode. The device with ZAZ electrodes had a PCE value of 3.53%, whereas the control device with ITO had a PCE value of 3.16%. ZnO layer between the glass and Ag NW network reduces the reflection of Ag NW network and increases the amount of absorbed light by the photoactive layer. The plasmonic effect of Ag NWs can be observable when a thin interfacial layer is applied on top of the network. Due to the plasmonic effect, the number of excitons and carriers increased when Ag NW network was placed near to the photoactive layer.

3.4. Experimental Details

3.4.1. Fabrication of Ag NW/PDMS Top Electrodes

Glass substrates are cut into rectangles with dimensions 2.45 cm \times 2.54 cm. Then, they are cleaned in acetone (99.8%), isopropyl alcohol (99.8%) and DI water (18.3 M Ω) for 15 minutes each in an ultrasonic bath. Subsequently, glass substrates are dried

under N₂ gas. They are placed on a hot plate and masked by a heat resistant tape. The mask defines 3 electrode regions with dimensions of 0.2 cm × 3 cm on a substrate. Afterwards spray coating is performed with a gun pressure of 2 atm onto the substrates heated to 120 °C. After spray coating, these samples are coated with PDMS polymer by spin coating. PDMS-assisted transfer of Ag NW network is carried out as mentioned in Chapter 2.

3.4.2. Fabrication of Inverted Solar Cells

In inverted OSCs, ITO is employed as the cathode. Three different inverted OSC were fabricated with the architecture ITO/ZnO/P3HT:PC₇₁BM/PEDOT:PSS/Ag NW/PDMS, ITO/ZnO/P3HT:ICBA/PEDOT:PSS/Ag NW/PDMS and ITO/ZnO/PBDB-T:ITIC/PEDOT:PSS/Ag NW/PDMS, respectively. Commercially available ITO (4-10 Ω/sq of sheet resistance and optical transmittance above 82% at a wavelength of 550 nm) on glass substrates are cut into 2.54 cm × 2.45cm pieces. The cathode area should be placed in the middle of glass substrate and have the dimensions of 2.54× 1.2 cm. So, this area is covered with a tape and remaining regions on the left and right-hand side of this area are left uncovered for etching process as shown schematically in Figure 3.5.

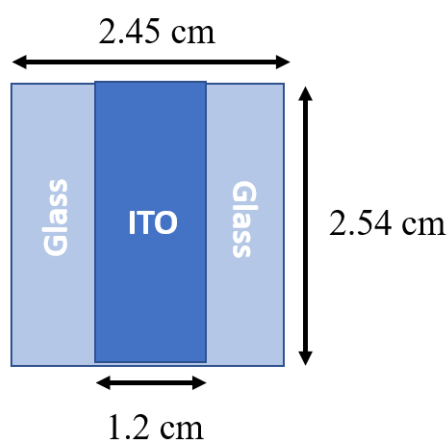


Figure 3. 5 Schematic illustration of bottom contact.

Then, an acidic solution containing 49 vol% hydrochloric acid (HCl) and 1 vol.% nitric acid (HNO₃) is prepared and ITO substrates are heated to 65 °C. ITO substrates are then etched in this solution for 4 minutes. The etched ITO samples are cleaned by sonication in toluene, detergent and isopropyl alcohol (99.8%). Then, ITO substrates are exposed to oxygen plasma to remove organic residuals on the surface. ZnO solution is prepared by mixing 0.4 g of zinc acetate dehydrate (Sigma Aldrich, ≥99.0%) and 0.10 ml ethanolamine (Sigma Aldrich, ≥98.0%) in 5 ml of 2-methoxyethanol (Sigma Aldrich, anhydrous, 99.8%) at room temperature, one day before the coating process. Afterwards, ZnO thin film is coated onto ITO by spin coating at 4000 rpm for 60 seconds. Then, the samples are annealed at 150 °C for 20 minutes. The photoactive layer consists of poly(3-hexylthiophene) (P3HT) as the donor and phenyl-C71-butyric acid methyl ester (PC₇₁BM) as the acceptor. Commercially available P3HT: PC₇₁BM is mixed at a ratio of 1:1 and dissolved with a concentration of 2.5% in dichlorobenzene. The solution is stirred within a glovebox for 8 hours at 70 °C. Then, the solution is filtered with a polytetrafluoroethylene (PTFE) filter with a pore size of 220 nm. Filtered solution is coated onto ZnO layer by spin coating at 750 rpm for 45 seconds in glovebox. Then, PEDOT:PSS (Ossila HTL) is filtered with a polyethersulfone (PES) filter having 450 nm pore size and spin coated on the photoactive layer at 2500 rpm for 60 seconds. PEDOT:PSS acts as the hole transport layer in this architecture. Finally, Ag NW/PDMS electrodes are placed on the device. The electrodes and the device are not fully overlapped. The electrode is slightly shifted to right-hand side in order to provide an area for contacts on the electrode. Then, the device is flipped over and Ag paste is applied on Ag NWs for contact points as shown in Figure 3.6. Additionally, a control device is fabricated by evaporating 100 nm thick Au metal as top electrode to compare device performances.

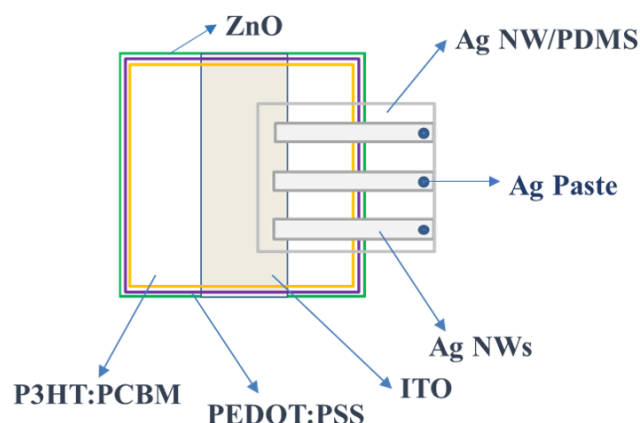


Figure 3. 6 Schematic top view of fabricated devices.

For ITO/ZnO/P3HT:ICBA/PEDOT:PSS/Ag NW/PDMS architecture, ITO and ZnO layers are prepared as aforementioned. Then, P3HT donor is mixed with ICBA acceptor at a ratio of 1:1. Then, the solution is spin coated onto ZnO in a glovebox and annealed at 140 °C for 10 minutes. After annealing, PEDOT:PSS solution is spin coated on the substrates and then, Ag NW/PDMS electrodes are placed. Contact points are prepared with Ag paste.

For ITO/ZnO/PBDB-T:ITIC/PEDOT:PSS/Ag NW/PDMS architecture, ITO and ZnO layers are prepared as aforementioned. Then, PBDB-T donor is mixed with ITIC acceptor at a ratio of 1:1 and dissolved in chlorobenzene at a concentration of 2%. 1 vol% of 1,8-diiodooctane is added as solvent addition. Dissolved photoactive layer solution is filtered using a PTFE filter with a pore size of 220 nm. Then, the solution is spin coated on ZnO in glovebox and annealed at 140 °C for 10 minutes. After annealing PEDOT:PSS solution is spin coated onto the substrates and then, Ag NW/PDMS electrodes are placed. Contact points are prepared with Ag paste.

3.5. Characterization Methods

3.5.1. Scanning Electron Microscopy (SEM)

Morphologies of the synthesized Ag NWs and prepared AgNW/PDMS samples are investigated using scanning electron microscope (SEM) (Nova NanoSEM 430). For SEM analysis, synthesized and purified Ag NWs were drop casted onto silicon wafers and no additional coating is applied. For Ag NW/PDMS samples Au coating is applied when necessary.

3.5.2. Atomic Force Microscopy (AFM)

Topography of Ag NW/PDMS samples are analyzed by AFM (Veeco MultiMode V). Measurements are performed in tapping mode.

3.5.3. Transmittance Measurements

UV-Vis characterization of Ag NW/PDMS electrodes are carried out with Bentham PVE300 photovoltaic characterization system.

3.5.4. Current – Voltage Characteristics

Photovoltaic characterization is carried out with an AM1.5G solar simulator having a power $100\text{mW}/\text{cm}^2$. Data are collected with Lab Tracer software.

3.6. Results

As-deposited Ag NW networks have high roughness values since they do not form a continuous thin film. Since high roughness leads to shorts in OSCs, it should be minimized to ensure a good device performance. When PDMS is coated over Ag NW network, it decreases the roughness by filling the voids between the Ag NWs. While as-deposited RMS roughness of Ag NWs was 54 nm [4], PDMS coated Ag NW thin films showed a RMS roughness value of 29 nm as stated in Chapter 2. An SEM image is provided in Figure 3.7 showing the morphology of Ag NW/PDMS electrodes.

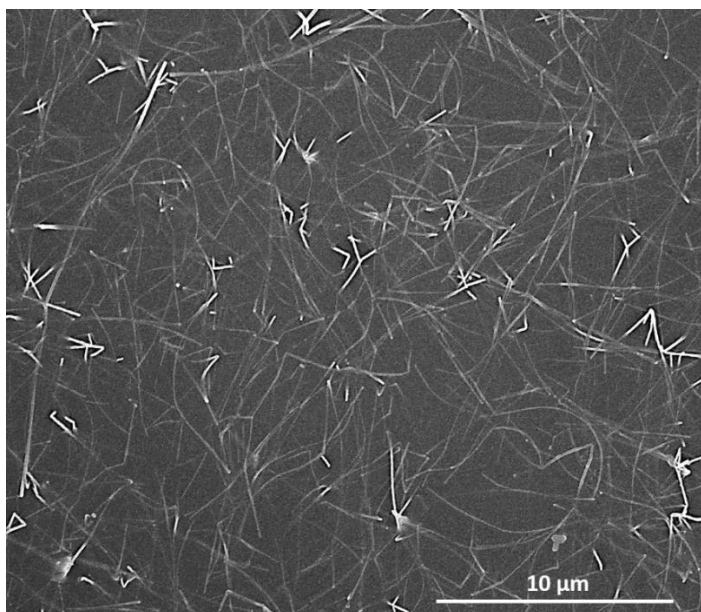


Figure 3. 7 SEM image of Ag NW/PDMS electrodes.

Transmittance measurements of Ag NW/PDMS electrodes were carried out in the wavelength range of 400-1000 nm with UV-Vis spectrometer. The optical transmittance of both Ag NW network and Ag NW/PDMS electrodes with sheet resistances of 10, 25 and 50 Ω /sq is shown before in Figures 2.12 (a), (b) and (c), respectively. The results are summarized at Table 2.1, which shows corresponding transmittance values at a wavelength of 550 nm. PDMS coating of Ag NWs leads to a 4% decrease in optical transmittance as compared to bare Ag NW networks.

Commercially available P3HT and PCBM donor:acceptor blend was chosen for the fabrication of devices. Ag NW/PDMS electrode was placed on the glass/ITO/ZnO/P3HT:PCBM/PEDOT:PSS cells. Schematic view of the fabricated devices and the photos of the electrodes and the finalized devices are shown in Figure 3.8.

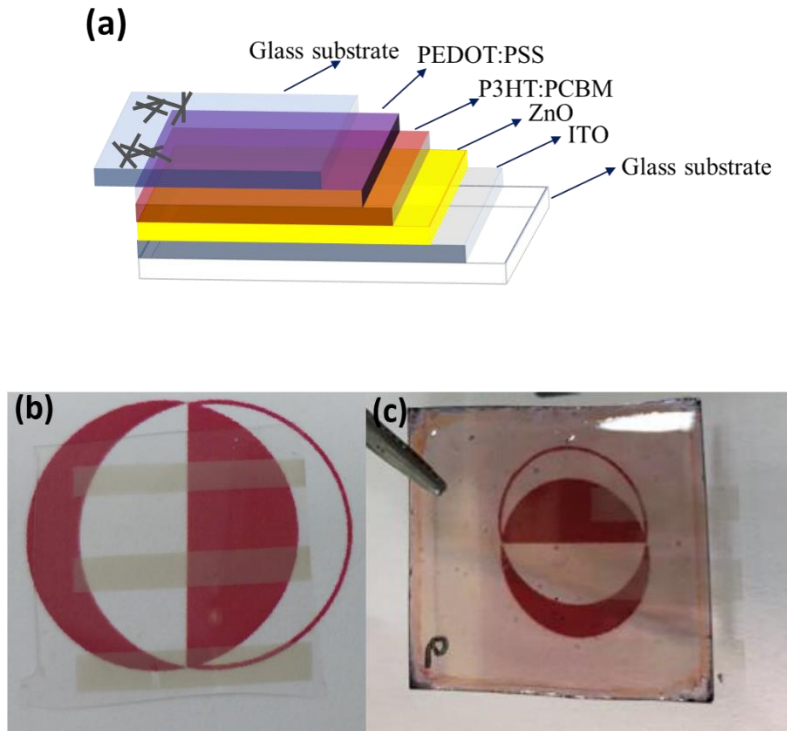


Figure 3. 8 Schematic view of the fabricated devices (a) side-view, photos of (b) Ag NW/PDMS electrode and (c) inverted OSC with Ag NW/PDMS top electrode.

Four different electrodes with sheet resistances of 10, 20, 30 and 50 Ω/sq are fabricated and placed onto the devices to investigate the effect of NW density on the device performance. The device fabricated with the electrode with a sheet resistance of 50 Ω/sq shorted. On the other hand, a correlation could not be found between device characteristics and sheet resistances of electrodes for 10, 20 and 30 Ω/sq electrodes. Each of these devices showed similar characteristics in terms of J_{SC} and PCE with promising performance. The PV performances of solar cells with electrodes having different sheet resistances are tabulated and provided in Table 3.2. Another important result that can be induced from Table 3.2 is that the illumination side has an effect on the device performance. V_{OC} remains constant, J_{SC} , FF and PCE decreases remarkably as the device is illuminated from Ag NW/ PDMS electrode side. This could simply be attributed to the lower transmittance of Ag NW/PDMS electrodes compared to ITO.

Table 3. 2 Performance of solar cells with electrodes having different sheet resistances.

Ag NW Resistance	Illumination side	V _{oc} (V)	J _{sc} (mA/cm ²)	FF (%)	PCE (%)
10 Ω/sq	ITO	0.55	6.15	0.57	1.93
10 Ω/sq	Ag Electrode	0.53	3.82	0.45	0.91
20 Ω/sq	ITO	0.58	5.61	0.62	2.02
20 Ω/sq	Ag Electrode	0.56	3.30	0.51	0.94
30 Ω/sq	ITO	0.57	6.57	0.48	1.81
30 Ω/sq	Ag Electrode	0.55	3.42	0.38	0.71
50 Ω/sq					Shorted

The PCE, V_{OC}, J_{SC} and FF of the highest performance device with the architecture of glass/ITO/ZnO/P3HT:PCBM/PEDOT:PSS/Ag NW-PDMS are 2.02 %, 0.58 V, 5.61 mA/cm², and 0.62, respectively. J – V is shown in Figure 3.9.

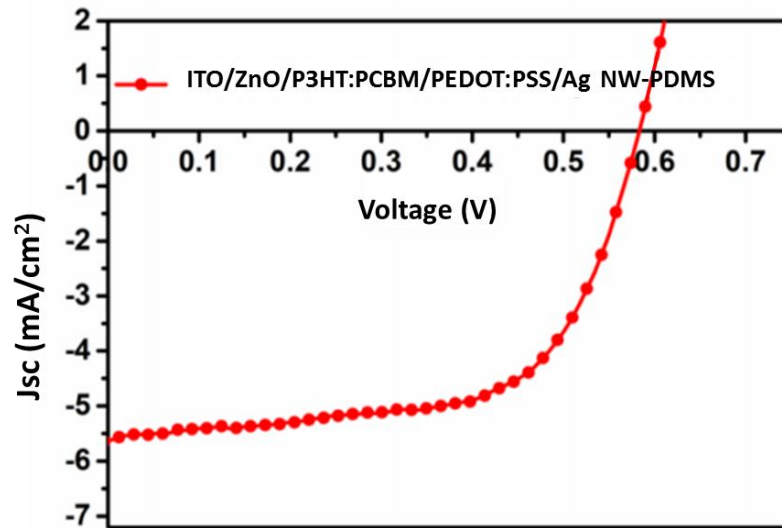


Figure 3. 9 J-V curve of glass/ITO/ZnO/P3HT:PCBM/PEDOT:PSS/Ag NW-PDMS (20 Ω/sq) structured IOS.

A control device is fabricated with 100 nm Au top electrode. The J-V measurements were carried out from the ITO side under 100 mW/cm² of AM 1.5G illumination. The corresponding J-V curve is provided in Figure 3.10. Table 3.3 shows a comparison between Ag NW/PDMS electrode with a sheet resistance of 20 Ω/sq and the control device with Au electrode. The V_{OC} and FF of both devices are comparable with each other. The difference occurs in J_{SC} value, which can be attributed to the optical properties of the electrode material. Au top electrode is opaque thus, it reflects back the incident light. Back-reflected light, in turn, enhances the device performance. On the other hand, incident light exit the device when it reaches to Ag NW/PDMS electrode due to its inherent transparency.

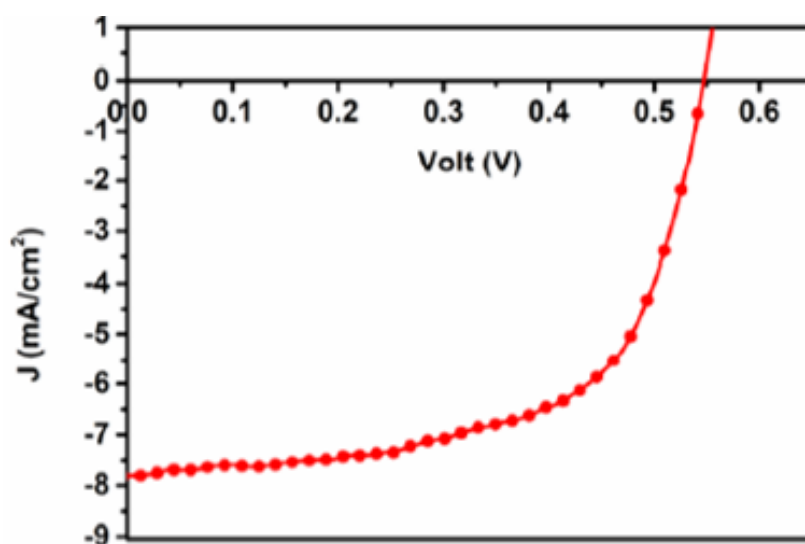


Figure 3. 10 J-V curve of glass/ITO/ZnO/P3HT:PCBM/PEDOT:PSS/Au structured IOSC.

Table 3. 3 Photovoltaic parameters of IOSCs with Ag NW/PDMS and Au anode.

Material	V _{OC} (V)	J _{SC} (mA/cm ²)	FF (%)	PCE (%)
Ag NW/PDMS	0.58	5.61	0.62	2.02
Au metal	0.54	7.84	0.62	2.62

A second architecture was designed by changing the acceptor in the polymer blend and keeping the rest of the structure as the same. Indene- C_{60} bisadduct (ICBA) polymer was used as acceptor due to its high LUMO value. It was expected to increase V_{OC} of the device since it is defined by the difference between energy the energy levels of HOMO of the donor and LUMO of the acceptor. The schematic view and the photo of the device is given in Figure 3.11 (a) and (b), respectively.

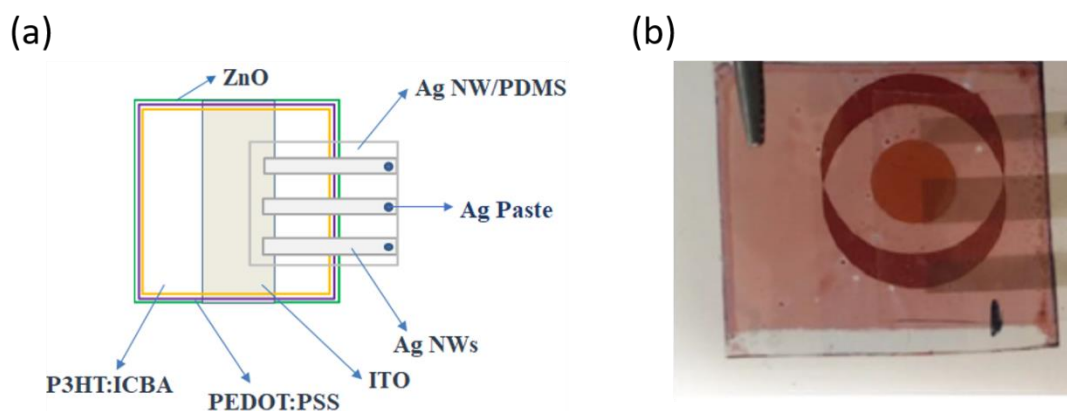


Figure 3. 11 (a) Schematic view, (b) photo of Glass/ITO/ZnO/P3HT:ICBA/PEDOT:PSS/Ag NW-PDMS devices.

The corresponding J-V curve and photovoltaic parameters are shown in Figure 3.12 and Table 3.4, respectively. The V_{OC} increased due to the increase in LUMO level of the acceptor as expected and PCE of the device was improved, as a result.

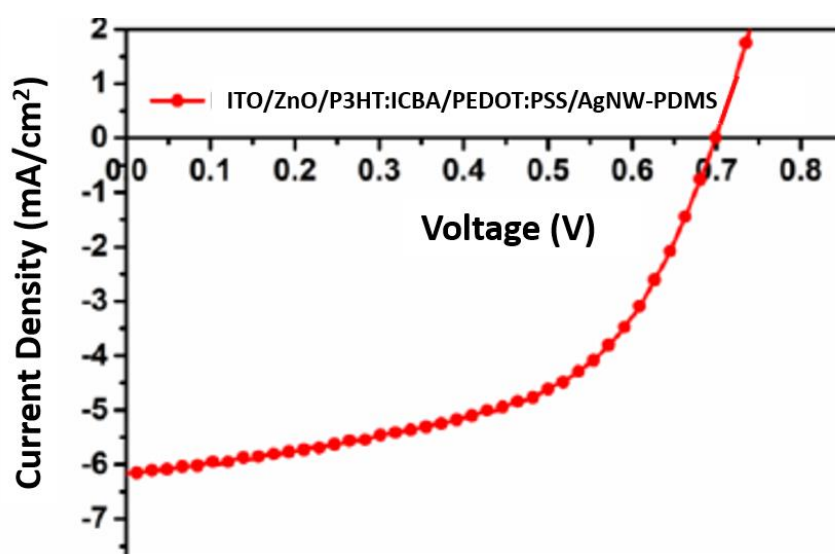


Figure 3. 12 J-V curve of glass/ITO/ZnO/P3HT:ICBA/PEDOT:PSS/Ag NW-PDMS structured IOSC.

Table 3. 4 Photovoltaic parameters of glass/ITO/ZnO/P3HT:ICBA/PEDOT:PSS/Ag NW-PDMS structured IOSC.

P3HT:ICBA	V_{oc} (V)	J_{sc} (mA/cm²)	FF (%)	PCE (%)
(1:1)	0.70	6.18	0.54	2.33

A third architecture is designed by changing the donor and the acceptor in the polymer blend and keeping the rest of the structure as the same. PBDB-T polymer is used as donor and ITIC polymer is used as acceptor material. The schematic view and a photo of the device is given in Figure 3.13 (a) and (b), respectively.

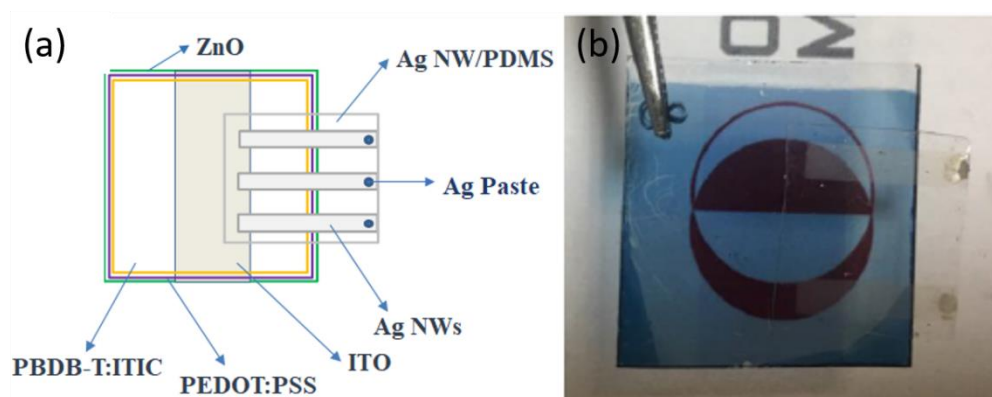


Figure 3. 13 (a) Schematic view and (b) photo of glass/ITO/ZnO/PBDB-T:ITIC/PEDOT:PSS/Ag NW-PDMS device.

The current – voltage characterization of the prepared solar cells are conducted under AM1.5G Solar Simulator. J – V characteristics of the mentioned solar cell is provided in Figure 3.14. Moreover, photovoltaic parameters are summarized in Table 3.5. The PCE, V_{oc} , J_{sc} and FF of the glass/ITO/ZnO/PBDB-T:ITIC/PEDOT:PSS/Ag NW-PDMS structured solar cell are 3.07 %, 0.85 V, 6.65 mA/cm², and 0.544, respectively.

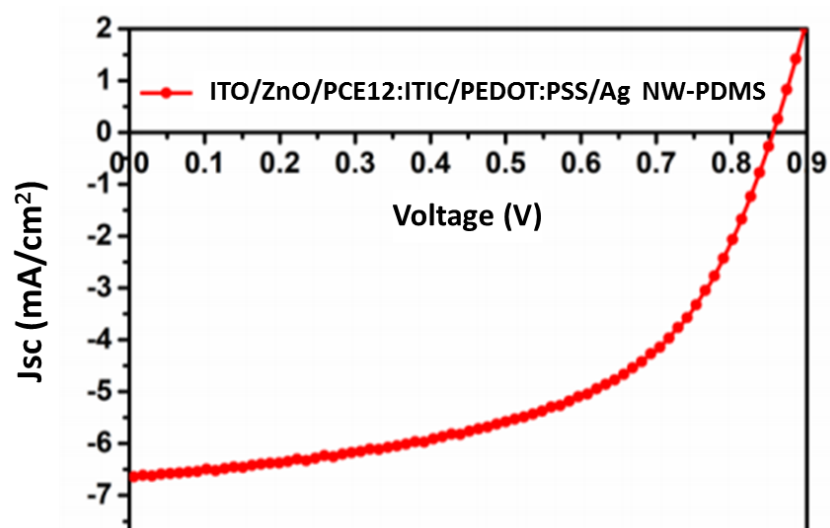


Figure 3. 14 J-V curve of glass/ITO/ZnO/PBDB-T:ITIC/PEDOT:PSS/Ag NW-PDMS structured solar cell device.

Table 3. 5 Photovoltaic parameters of glass/ITO/ZnO/PBDB-T:ITIC/PEDOT:PSS/Ag NW-PDMS structured solar cell device.

PBDB-T:ITIC	Voc (V)	Jsc (mA/cm²)	FF (%)	PCE (%)
(1:1)	0.85	6.65	0.544	3.07

CHAPTER 4

TRANSPARENT AND CONDUCTING Ag NW/PDMS ELECTRODES FOR PEROVSKITE SOLAR CELLS

4.1. Introduction

Perovskite solar cells (PSC) has emerged recently as a cheap, solution processable alternative in photovoltaic industry. Perovskite is a crystal structure having a specific molecular formula of ABX_3 , where X is denoted for oxygen or halogen elements. The larger A cation is located at cubic octahedral site neighbored by twelve X anions, whereas the smaller B cation is located on octahedral site neighbored by six X anions. $CH_3NH_3PbX_3$ (X: Br, I) was applied as a sensitizer in dye-sensitized solar cells for the first time in 2009 by Kojima et al. and resulted in a power conversion efficiency of 3.8% [76]. This is followed by the demonstration of a PCE of 6.5% by utilizing $CH_3NH_3PbI_3$ based perovskites by Im et al [77]. However, there were ongoing instability problems of these devices. Then, the first long term stable PSC showing a PCE of 9.7% was reported by Kim et al [78]. Rapid progresses were achieved over the years and the PCE of perovskite solar cells has exceeded 22% in a short period of time [79].

4.2. Device Architecture and Operation Principles

PCS structure mainly consists of a perovskite photoactive layer sandwiched in between two interfacial layers and two electrodes. Interfacial layers are called as electron transport material (ETM) and hole transport material (HTM). They promote charge transport between the photoactive layer and electrodes. One of the electrodes is transparent conductive oxide such as ITO or FTO. The other electrode is fabricated by evaporating aluminum, gold or silver metals. There are two different structural configurations for PSCs called as normal geometry (n-i-p) and inverted geometry (p-

i-n) as shown schematically in Figure 4.1. The difference between these two geometries is the portion of the device that is subjected to the incident light. There is another structural classification based on the morphology of the layers and they are called as mesoporous or planar structures.

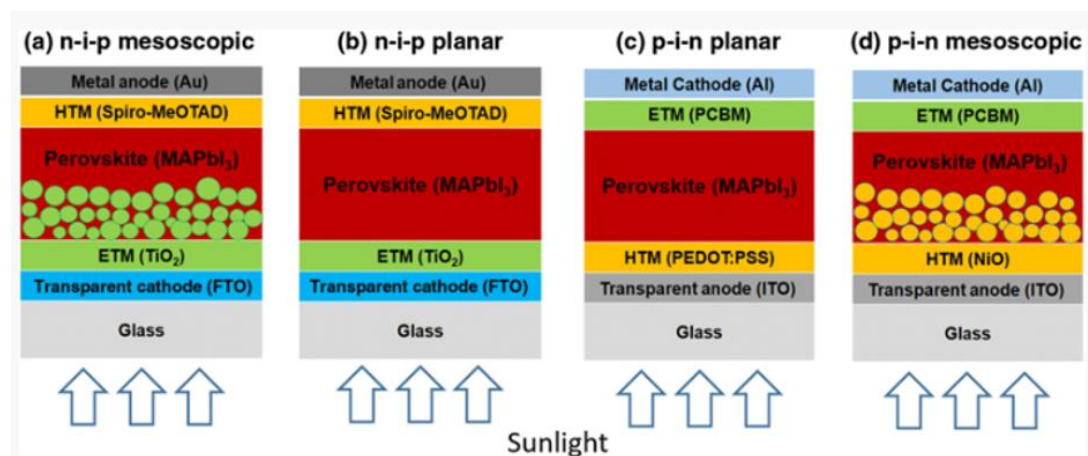


Figure 4. 1 Device structure of PSCs having (a) normal mesoscopic, (b) normal planar, (c) inverted planar and (d) inverted mesoscopic geometries [80].

The mesoscopic n-i-p architecture is the original and still mostly utilized perovskite architecture. Mesoscopic structure decreases the carrier transport distance and hence enhances the charge collection ability of the device. Moreover, it absorbs photons efficiently due to light scattering. The planar architecture was evolved from mesoscopic structure during layer optimizations. Although planar n-i-p structures have shown better results in terms of J_{SC} and V_{OC} , they undergo significant hysteresis behavior as compared to mesoscopic n-i-p architecture [81].

The p-i-n structure can be obtained by changing the deposition order of HTM and ETM. Planar p-i-n devices are advantageous in terms of low temperature processing, minor hysteresis behavior and a high efficiency of 18% [82].

The first PSC structure involved a mesoporous TiO₂ layer. Thus, it was believed that the photogenerated charge carriers was injected to the wide bandgap of TiO₂ as in dye-

sensitized solar cells, which are ancestors of this technology. However, it was revealed that perovskite itself was both hole and electron conductor after the fabrication of devices without ETM and HTM layers [83]. The solar cells having the best performance were fabricated using $\text{CH}_3\text{NH}_3\text{PbI}_3$ with a bandgap of 1.55 eV, which is very close to optimal bandgap value of 1.4 eV to obtain a maximum efficiency from a solar cell [84]. Moreover, high extinction coefficient of perovskite materials provides a good absorption in a broader spectrum at low film thicknesses. Decreased film thicknesses resulted in shorter lengths for charge diffusion, reduced recombination rate, reduced energetic losses and increased voltage of the device. Furthermore, low exciton binding energy, which results in a high number of holes and electrons in perovskite leads to higher PCE values.

Once charge carriers are generated, they should be transported through contacts to be extracted. Metal halide perovskites have long diffusion lengths and lifetime of charge carriers. For instance, $\text{CH}_3\text{NH}_3\text{PbI}_3$ has a diffusion length of 100 nm, whereas $\text{CH}_3\text{NH}_3\text{PbI}_{3-x}\text{Cl}_x$ has a diffusion length above 1 μm [83].

4.3. Experimental Details

Mesoporous perovskite solar cells having normal geometry were examined with Ag metal and Ag NW/PDMS electrodes in this work.

4.3.1. Fabrication of Perovskite Solar Cells

FTO on glass was used as the substrate. These were cleaned in acetone, isopropyl alcohol, hellmanex and deionized water for 10 minutes in an ultrasonic bath. Then, cleaned substrates were dried under N_2 gas and cleaned under UV-ozone for 10 minutes. k- TiO_2 layer was coated onto the substrate in order to obtain desired n-i-p structure. After annealing at 500 °C for 30 minutes, samples were immersed in 20 mM TiCl_4 solution to modify k- TiO_2 surface. Then, 18 NR-T titanium dioxide material was dissolved in ethanol (150 mg/ml) and spin coated over k- TiO_2 layer to obtain a mesoporous structure. Afterwards, samples were annealed at 500 °C and placed into glovebox. Following steps including coating of the perovskite layer and hole transport

layer were carried out in glovebox. The stoichiometry of perovskite layer was $(\text{FA}_{0.79}\text{MA}_{0.16}\text{Cs}_{0.05})_{0.97}\text{Pb}(\text{I}_{0.84}\text{Br}_{0.16})_{2.97}$. To obtain this triple cation structure (FAMACs), 172 mg of formamidinium iodide (FAI), 507 mg of lead iodide (PbI_2), 22.4 mg of methylammonium bromide (MABr) and 73.4 mg of lead bromide (PbBr_2) chemicals are weighed in molar ratio of 1:1.1:0.2:0.2, respectively and dissolved in 1 ml of dimethylformamide:dimethyl sulfoxide (DMF:DMSO, 4:1) solution. Then, 45 μl of cesium iodide (CsI) stock solution (1.5 M, DMSO) is added to the solution. The obtained perovskite solution is spin coated with a two-step procedure having the parameters 1000 rpm for 10 seconds and 4000 rpm for 20 seconds. In order to obtain pin-hole free and high crystal quality perovskite layers, 100 μl chlorobenzene is dropped on perovskite just before the end of spin coating. After annealing at 100 °C for 1 hour, black colored perovskite thin films are obtained. Spiro-OMeTAD layer is coated onto perovskite thin films to obtain p-type layer. 72 mg of Spiro-OMeTAD is dissolved in chlorobenzene and doped with 30 μl 4-tert-butylpyridine (t-BP), 18 μl of Li-TFSI (520 mg/ml, in acetonitrile) and 14 μl of FK209 Co(III)PF_6 (300 mg/ml, in acetonitrile) salt solutions by stirring at room temperature. Then the solution is spin coated onto perovskite at 4000 rpm for 30 seconds. Lastly, a 120 nm thick Ag electrode is thermally evaporated onto the control devices.

4.3.2. Fabrication of Ag NW/PDMS Electrodes

Ag NW/PDMS electrodes are fabricated as explained in Chapter 2 and placed on perovskite solar cells as top electrodes.

4.4. Characterization Methods

4.4.1. Scanning Electron Microscopy (SEM)

Synthesized Ag NWs and prepared AgNW/PDMS samples were investigated under scanning electron microscope (SEM) (Nova NanoSEM 430). Synthesized and purified

Ag NWs were drop casted on silicon wafer and no additional coating was applied. For Ag NW/PDMS samples Au coating was applied when necessary.

4.4.2. Photovoltaic Characterization

Photovoltaic characterization was carried out with an AM1.5G solar simulator having a power 100 mW/cm^2 .

4.5. Results

Mesoporous perovskite solar cells with normal geometry are fabricated using Ag NW/PDMS electrodes as cathodes. The SEM image of the electrode and photographs of Ag NW/PDMS electrodes and final device are given in Figure 4.2.

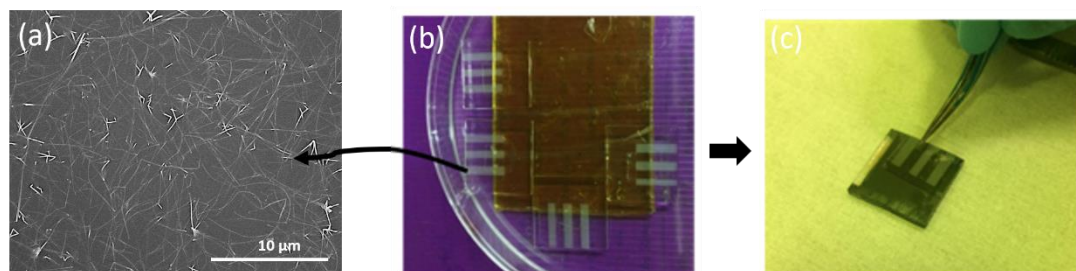


Figure 4. 2 (a) SEM image of Ag NW/PDMS electrodes, photo of (b) Ag NW/PDMS electrodes and (c) fabricated perovskite solar cell.

A mesoporous titanium dioxide layer consisting of $k\text{-TiO}_2/m\text{-TiO}_2$ is utilized as electron transport layer to increase the efficiency of solar cell. Schematic illustration for the fabricated devices is given in Figure 4.3.

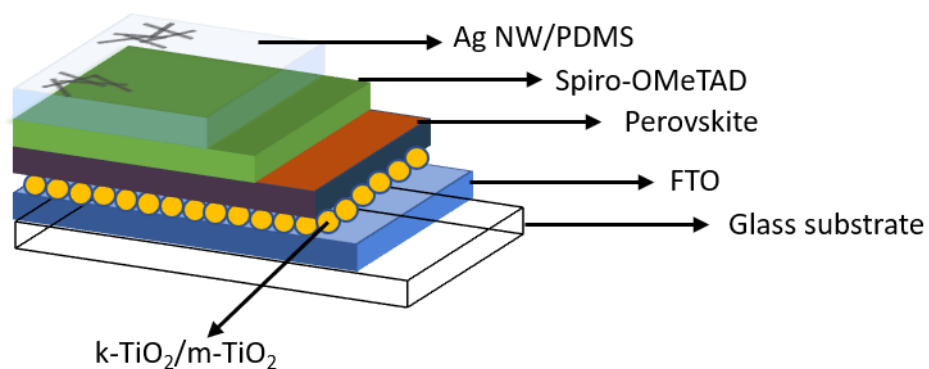


Figure 4. 3 Schematic illustration of the device architecture.

Photovoltaic characterization of control devices with evaporated Ag metal cathodes, resulted in an efficiency value of 17.7%. Figure 4.4 shows J-V curve of control device. Current density, open circuit voltage and fill factor were 21.2 mA/cm², 1.15 V and 72.6%, respectively.

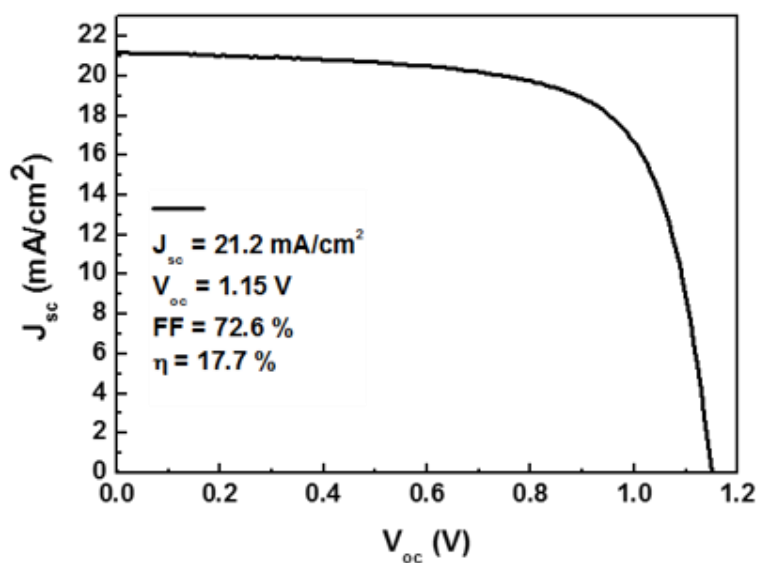


Figure 4. 4 J-V curve of the control device.

The device with Ag NW/PDMS cathode has achieved an efficiency of 6.5% as shown in Figure 4.5.

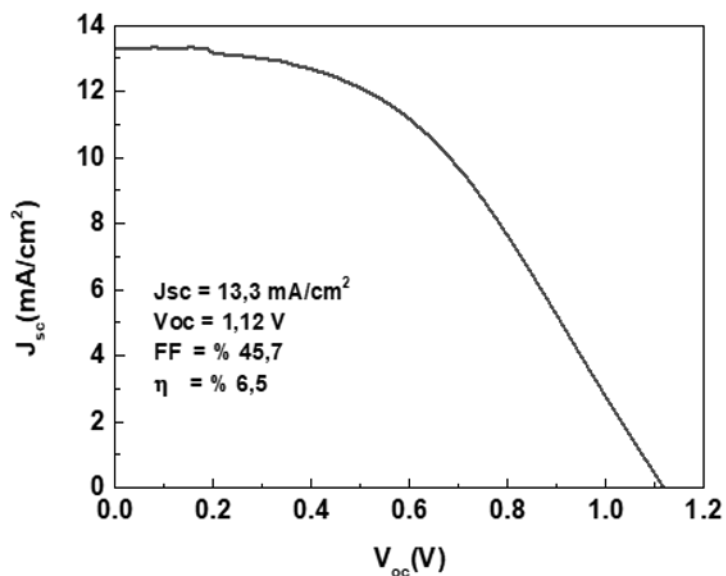


Figure 4. 5 J-V curve of perovskite solar cell with Ag NW/PDMS cathode.

There is no significant change in V_{oc} values of both devices; however, the difference comes from J_{sc} and FF. High amount of series resistance can be addressed to the FF decrease. The series resistance represents a collective resistance, which is based on the resistance of all the layers or interfaces and the conductivity of the layers of the cell including the electrodes. Thus, it can be decreased by the matching between the electrode and HTL by modifying the surfaces either with the help of chemicals or oxygen plasma treatment. On the other hand, low J_{sc} can be addressed to the roughness and optical transmittance of Ag NWs. A detailed parametric study can be performed with different NW densities to observe the potential effect on the device performance.

As can be seen, the very first results of this study are highly promising and can be improved.

CHAPTER 5

CONCLUSIONS AND FUTURE RECOMMENDATIONS

5.1. Conclusions

This thesis is focused on a facile and solution processed transfer method of Ag NW networks via PDMS for the fabrication of Ag NW/PDMS electrodes, which were then utilized in organic and perovskite solar cells.

In the first part of this thesis, Ag NWs were synthesized with polyol method followed by purification. Synthesized Ag NWs have the average dimensions of 60 nm in diameter and 8 μm in length. Then, Ag NWs were spray coated onto glass substrates and this was followed by spin coating of PDMS over Ag NW network. As PDMS layer was peeled of glass substrates, the transfer of Ag NW network to PDMS surface was achieved. PDMS-assisted transfer provides approximately 100% of transfer efficiency. Analysis carried on glass substrates has revealed that, only a few individual Ag NWs remain on the surface, whereas there was no evidence on the network structure.

In the second part, Ag NW/PDMS electrodes were used as top electrodes of inverted OSCs. Motivation behind this was to replace evaporated metal electrodes for obtaining semi-transparent devices. A sheet resistance optimization study was carried out for Ag NW/PDMS electrodes and revealed that each of these electrodes had characteristics in terms of J_{SC} and PCE, with promising device performance. Moreover, device performance was affected by the illumination side during photovoltaic characterization. When device was illuminated from Ag NW/PDMS side, PCE of the device was found to decrease remarkably.. Lastly, three different OSC architectures were fabricated with Ag NW/PDMS electrodes. Accordingly, cells based on glass/ITO/ZnO/P3HT:PCBM/PEDOT:PSS/Ag NW-PDMS architecture has shown a PCE of 2.02%. Two other device architectures which are

glass/ITO/ZnO/P3HT:ICBA/PEDOT:PSS/Ag NW-PDMS and glass/ITO/ZnO/PBDB-T:ITIC/PEDOT:PSS/Ag NW-PDMS were also demonstrated, where PCE values of 2.33% and 3.07% were obtained, respectively. Efficiencies of OSCs having Ag NW/PDMS electrodes were slightly lower than that of control devices, yet performance of Ag NW/PDMS electrodes are still promising and can be improved.

In the final part, Ag NW/PDMS electrodes was demonstrated as top electrodes for semi-transparent PCS. A perovskite solar cell based on glass/FTO/k-TiO₂/m-TiO₂/Perovskite/Spiro-OMeTAD/Ag NW/PDMS architecture was demonstrated and a PCE of 6.5% was obtained, whereas the control device based on glass/FTO/k-TiO₂/m-TiO₂/Perovskite/Spiro-OMeTAD/Ag showed a PCE of 17.7%.

5.2. Future Recommendations

Transparency of Ag NW/PDMS electrodes can be enhanced by utilizing longer Ag NWs. This is due to the presence of a smaller number of junction points on a defined area since the conductive pathway for electron transfer can be ensured with the utilization of less Ag NWs when longer nanowires are used. This can be also helpful for reducing roughness of Ag NW networks further.

Interfacial matching behavior between solar cell devices and Ag NW/PDMS electrodes can be examined to enhance device performance. Especially, matching of PDMS with the underlying surface can be further improved by modifying its surface by either chemical or physical means such as applying oxygen plasma prior to integration to devices. Secondly, introducing interlayers to the electrode structure such as building tri-layer geometries can improve the overall conductivity and J_{SC} of the devices.

REFERENCES

- [1] IPCC, *Summary for Policymakers. In: Global warming of 1.5°C. An IPCC Special Report on the impacts of global warming.* 2018.
- [2] U. S. D. of Energy, “The History of Solar Technology,” *Pennyhill Press*, 2013.
- [3] W. Gaynor, G. F. Burkhard, M. D. McGehee, and P. Peumans, “Smooth nanowire/polymer composite transparent electrodes,” *Adv. Mater.*, vol. 23, no. 26, pp. 2905–2910, 2011.
- [4] S. Coskun, E. Selen Ates, and H. Emrah Unalan, “Optimization of silver nanowire networks for polymer light emitting diode electrodes,” *Nanotechnology*, vol. 24, no. 12, 2013.
- [5] C. Celle, C. Mayousse, E. Moreau, H. Basti, A. Carella, and J. P. Simonato, “Highly flexible transparent film heaters based on random networks of silver nanowires,” *Nano Res.*, vol. 5, no. 6, pp. 427–433, 2012.
- [6] Q. Huang *et al.*, “Highly flexible and transparent film heaters based on polyimide films embedded with silver nanowires,” *RSC Adv.*, vol. 5, no. 57, pp. 45836–45842, 2015.
- [7] M. A. Shinde, D. Lee, B. Kim, and H. Kim, “Highly conductive and smooth surfaced flexible transparent conductive electrode based on silver nanowires,” *Thin Solid Films*, vol. 685, no. January, pp. 366–371, 2019.
- [8] T. Kim, Y. W. Kim, H. S. Lee, H. Kim, W. S. Yang, and K. S. Suh, “Uniformly interconnected silver-nanowire networks for transparent film heaters,” *Adv. Funct. Mater.*, vol. 23, no. 10, pp. 1250–1255, 2013.
- [9] J. W. Lim *et al.*, “Mechanical integrity of flexible Ag nanowire network electrodes coated on colorless PI substrates for flexible organic solar cells,” *Sol. Energy Mater. Sol. Cells*, vol. 105, pp. 69–76, 2012.
- [10] C. C. Chen *et al.*, “Visibly transparent polymer solar cells produced by solution processing,” *ACS Nano*, vol. 6, no. 8, pp. 7185–7190, 2012.
- [11] W. Gaynor, J. Y. Lee, and P. Peumans, “Fully solution-processed inverted polymer solar cells with laminated nanowire electrodes,” *ACS Nano*, vol. 4, no. 1, pp. 30–34, 2010.
- [12] J. Y. Lee, S. T. Connor, Y. Cui, and P. Peumans, “Solution-processed metal nanowire mesh transparent electrodes,” *Nano Lett.*, vol. 8, no. 2, pp. 689–692, 2008.
- [13] W. Hu, X. Niu, R. Zhao, and Q. Pei, “Elastomeric transparent capacitive

- sensors based on an interpenetrating composite of silver nanowires and polyurethane,” *Appl. Phys. Lett.*, vol. 102, no. 8, 2013.
- [14] X. Guo, Y. Ma, Y. Wang, and L. Tong, “Nanowire plasmonic waveguides, circuits and devices,” *Laser Photonics Rev.*, vol. 7, no. 6, pp. 855–881, 2013.
- [15] S. Ye, A. R. Rathmell, Z. Chen, I. E. Stewart, and B. J. Wiley, “Metal Nanowire Networks : The Next Generation of Transparent Conductors,” pp. 6670–6687, 2014.
- [16] B. Azzopardi, C. J. M. Emmott, A. Urbina, F. C. Krebs, J. Mutale, and J. Nelson, “Economic assessment of solar electricity production from organic-based photovoltaic modules in a domestic environment,” *Energy Environ. Sci.*, vol. 4, no. 10, pp. 3741–3753, 2011.
- [17] A. Kumar and C. Zhou, “The Race To Replace Tin-Doped Indium Oxide : Which Material Will Win ?,” vol. 4, no. 1, pp. 11–14, 2010.
- [18] D. S. Hecht, L. Hu, and G. Irvin, “Emerging transparent electrodes based on thin films of carbon nanotubes, graphene, and metallic nanostructures,” *Adv. Mater.*, vol. 23, no. 13, pp. 1482–1513, 2011.
- [19] K. Ellmer, “Past achievements and future challenges in the development of optically transparent electrodes,” *Nat. Photonics*, vol. 6, no. 12, pp. 809–817, 2012.
- [20] T. Fang, A. Konar, H. Xing, and D. Jena, “Carrier statistics and quantum capacitance of graphene sheets and ribbons,” *Appl. Phys. Lett.*, vol. 91, no. 9, p. 092109, Aug. 2007.
- [21] K. S. Novoselov, A. K. Geim, S. V Morozov, and D. Jiang, “Electric Field Effect in Atomically Thin Carbon Films,” vol. 306, no. October, pp. 666–669, 2004.
- [22] A. I. Hofmann, E. Cloutet, and G. Hadziioannou, “Materials for Transparent Electrodes: From Metal Oxides to Organic Alternatives,” *Adv. Electron. Mater.*, vol. 4, no. 10, 2018.
- [23] D. Zhang *et al.*, “Transparent, conductive, and flexible carbon nanotube films and their application in organic light-emitting diodes,” *Nano Lett.*, vol. 6, no. 9, pp. 1880–1886, 2006.
- [24] S. Park, M. Vosguerichian, and Z. Bao, “A review of fabrication and applications of carbon nanotube film-based flexible electronics,” *Nanoscale*, vol. 5, no. 5, pp. 1727–1752, 2013.
- [25] H.-Z. Geng, D. S. Lee, K. K. Kim, G. H. Han, H. K. Park, and Y. H. Lee, “Absorption spectroscopy of surfactant-dispersed carbon nanotube film: Modulation of electronic structures,” *Chem. Phys. Lett.*, vol. 455, no. 4–6, pp.

275–278, Apr. 2008.

- [26] L. Groenendaal, G. Zotti, P. H. Aubert, S. M. Waybright, and J. R. Reynolds, “Electrochemistry of poly(3,4-alkylenedioxythiophene) derivatives,” *Adv. Mater.*, vol. 15, no. 11, pp. 855–879, 2003.
- [27] A. M. Nardes, M. Kemerink, M. M. de Kok, E. Vinken, K. Maturova, and R. A. J. Janssen, “Conductivity, work function, and environmental stability of PEDOT:PSS thin films treated with sorbitol,” *Org. Electron.*, vol. 9, no. 5, pp. 727–734, Oct. 2008.
- [28] J. Zou, H. L. Yip, S. K. Hau, and A. K. Y. Jen, “Metal grid/conducting polymer hybrid transparent electrode for inverted polymer solar cells,” *Appl. Phys. Lett.*, vol. 96, no. 20, 2010.
- [29] Y. Jang, J. Kim, and D. Byun, “Invisible metal-grid transparent electrode prepared by electrohydrodynamic (EHD) jet printing,” *J. Phys. D: Appl. Phys.*, vol. 46, no. 15, p. 155103, Apr. 2013.
- [30] K. D. M. Rao, C. Hunger, R. Gupta, G. U. Kulkarni, and M. Thelakkat, “A cracked polymer templated metal network as a transparent conducting electrode for ITO-free organic solar cells,” *Phys. Chem. Chem. Phys.*, vol. 16, no. 29, pp. 15107–15110, 2014.
- [31] S. De *et al.*, “Silver Nanowire Networks as Flexible, Transparent, Conducting Films: Extremely High DC to Optical Conductivity Ratios.,” *ACS Nano*, vol. 3, no. 7, pp. 1767–1774, 2009.
- [32] A. Bid, A. Bora, and A. K. Raychaudhuri, “Temperature dependence of the resistance of metallic nanowires of diameter ≥ 15 nm: Applicability of Bloch-Grüneisen theorem,” *Phys. Rev. B - Condens. Matter Mater. Phys.*, vol. 74, no. 3, pp. 1–8, 2006.
- [33] G. Haacke, “New figure of merit for transparent conductors,” *J. Appl. Phys.*, vol. 47, no. 9, pp. 4086–4089, Sep. 1976.
- [34] T. Sannicolo, M. Lagrange, A. Cabos, C. Celle, J. Simonato, and D. Bellet, “Metallic Nanowire-Based Transparent Electrodes for Next Generation Flexible Devices : a Review,” *Small*, vol. 12, no. 44, pp. 6052–6075, 2016.
- [35] M. Lagrange, D. P. Langley, G. Giusti, C. Jiménez, Y. Bréchet, and D. Bellet, “Optimization of silver nanowire-based transparent electrodes: Effects of density, size and thermal annealing,” *Nanoscale*, vol. 7, no. 41, pp. 17410–17423, 2015.
- [36] S. Sorel, D. Bellet, and J. N. Coleman, “Relationship between material properties and transparent heater performance for both bulk-like and percolative nanostructured networks,” *ACS Nano*, vol. 8, no. 5, pp. 4805–4814, 2014.

- [37] D. Doganay, S. Coskun, S. P. Genlik, and H. E. Unalan, "Silver nanowire decorated heatable textiles," *Nanotechnology*, vol. 27, no. 43, p. 435201, Oct. 2016.
- [38] M. Reinhard, R. Eckstein, A. Slobodskyy, U. Lemmer, and A. Colsmann, "Solution-processed polymer-silver nanowire top electrodes for inverted semi-transparent solar cells," *Org. Electron. physics, Mater. Appl.*, vol. 14, no. 1, pp. 273–277, 2013.
- [39] J. Kwon *et al.*, "Recent progress in silver nanowire based flexible/wearable optoelectronics," *J. Mater. Chem. C*, vol. 6, no. 28, pp. 7445–7461, 2018.
- [40] M. Nogi, N. Komoda, K. Otsuka, and K. Suganuma, "Foldable nanopaper antennas for origami electronics," *Nanoscale*, vol. 5, no. 10, pp. 4395–4399, 2013.
- [41] Y. Zhou, S. H. Yu, C. Y. Wang, X. G. Li, Y. R. Zhu, and Z. Y. Chen, "A novel ultraviolet irradiation photoreduction technique for the preparation of single-crystal Ag nanorods and Ag dendrites," *Adv. Mater.*, vol. 11, no. 10, pp. 850–852, 1999.
- [42] Y. Zhou, S. H. Yu, X. P. Cui, G. Y. Wang, and Z. Y. Chen, "Formation of silver nanowires by a novel solid-liquid phase arc discharge method," *Chem. Mater.*, vol. 11, no. 3, pp. 545–546, 1999.
- [43] X.-Y. Sun, F.-Q. Xu, Z.-M. Li, and W.-H. Zhang, "Cyclic voltammetry for the fabrication of high dense silver nanowire arrays with the assistance of AAO template," *Mater. Chem. Phys.*, vol. 90, no. 1, pp. 69–72, Mar. 2005.
- [44] J. Xu, J. Hu, C. Peng, H. Liu, and Y. Hu, "A simple approach to the synthesis of silver nanowires by hydrothermal process in the presence of gemini surfactant," *J. Colloid Interface Sci.*, vol. 298, no. 2, pp. 689–693, Jun. 2006.
- [45] Y. Sun, Y. Yin, B. T. Mayers, T. Herricks, and Y. Xia, "Uniform silver nanowires synthesis by reducing AgNO₃ with ethylene glycol in the presence of seeds and poly(vinyl pyrrolidone)," *Chem. Mater.*, vol. 14, no. 11, pp. 4736–4745, 2002.
- [46] S. Coskun, B. Aksoy, and H. E. Unalan, "Polyol synthesis of silver nanowires: An extensive parametric study," *Cryst. Growth Des.*, vol. 11, no. 11, pp. 4963–4969, 2011.
- [47] D. Langley, G. Giusti, C. Mayousse, C. Celle, D. Bellet, and J. Simonato, "Flexible transparent conductive materials based on silver nanowire networks : a review," *Nanotechnology*, vol. 24, no. 452001, 2013.
- [48] L. Hu, H. S. Kim, J. Y. Lee, P. Peumans, and Y. Cui, "Scalable coating and properties of transparent, flexible, silver nanowire electrodes," *ACS Nano*, vol. 4, no. 5, pp. 2955–2963, 2010.

- [49] A. R. Madaria, A. Kumar, F. N. Ishikawa, and C. Zhou, “Uniform, highly conductive, and patterned transparent films of a percolating silver nanowire network on rigid and flexible substrates using a dry transfer technique,” *Nano Res.*, vol. 3, no. 8, pp. 564–573, 2010.
- [50] A. R. Madaria, A. Kumar, and C. Zhou, “Large scale , highly conductive and patterned transparent films of silver nanowires on arbitrary substrates and their application in touch screens,” *Nanotechnology*, vol. 22, no. 245201, 2011.
- [51] J. A. Mendez-Gamboa, R. Castro-Rodriguez, I. V. Perez-Quintana, R. A. Medina-Esquivel, and A. Martel-Arbelo, “A figure of merit to evaluate transparent conductor oxides for solar cells using photonic flux density,” *Thin Solid Films*, vol. 599, pp. 14–18, Jan. 2016.
- [52] R. Jarrett, D. Dawson, K. Roelich, and P. Purnell, “Calculating material criticality of transparent conductive electrodes used for thin film and third generation solar cells,” *2014 IEEE 40th Photovolt. Spec. Conf. PVSC 2014*, pp. 1436–1441, 2014.
- [53] J. Ma, S.-Y. Li, J. Zhao, and H.-L. Ma, “Preparation and properties of indium tin oxide films deposited on polyester substrates by reactive evaporation,” *Thin Solid Films*, vol. 307, no. 1–2, pp. 200–202, Oct. 1997.
- [54] L. K. Wang, J. J. Chen, J. Y. Yu, H. L. Zhao, and J. K. Yang, “Highly textured spray-deposited SnO₂:F films with high haze for solar cells,” *Vacuum*, vol. 169, p. 108879, Nov. 2019.
- [55] V. Gowrishankar, D. Hutton, C. Fluhrer, and N. Dasgupta, “Making photovoltaic power competitive with grid power,” *Conf. Rec. 2006 IEEE 4th World Conf. Photovolt. Energy Conversion, WCPEC-4*, vol. 2, pp. 2532–2535, 2007.
- [56] ASTM G173-03(2012), “Standard Tables for Reference Solar Spectral Irradiances: Direct Normal and Hemispherical on 37° Tilted Surface,” *Astm*, vol. 03, no. Reapproved 2012, pp. 1–21, 2013.
- [57] D. Chirvase, J. Parisi, J. C. Hummelen, and V. Dyakonov, “Influence of nanomorphology on the photovoltaic action of polymer–fullerene composites,” *Nanotechnology*, vol. 15, no. 9, pp. 1317–1323, Sep. 2004.
- [58] H. Hoppe *et al.*, “Nanoscale morphology of conjugated polymer/fullerene-based bulk-heterojunction solar cells,” *Adv. Funct. Mater.*, vol. 14, no. 10, pp. 1005–1011, 2004.
- [59] M. D. Irwin, D. B. Buchholz, A. W. Hains, R. P. H. Chang, and T. J. Marks, “p-Type semiconducting nickel oxide as an efficiency-enhancing anode interfacial layer in polymer bulk-heterojunction solar cells,” *Proc. Natl. Acad. Sci.*, vol. 105, no. 8, pp. 2783–2787, Feb. 2008.

- [60] D. W. Zhao, X. W. Sun, C. Y. Jiang, A. K. K. Kyaw, G. Q. Lo, and D. L. Kwong, "Efficient tandem organic solar cells with an Al/ MoO₃ intermediate layer," *Appl. Phys. Lett.*, vol. 93, no. 8, 2008.
- [61] V. Shrotriya, G. Li, Y. Yao, C.-W. Chu, and Y. Yang, "Transition metal oxides as the buffer layer for polymer photovoltaic cells," *Appl. Phys. Lett.*, vol. 88, no. 7, p. 073508, Feb. 2006.
- [62] M. Hösel, D. Angmo, and F. C. Krebs, *Organic solar cells (OSCs)*. 2013.
- [63] M. Jørgensen, K. Norrman, and F. C. Krebs, "Stability/degradation of polymer solar cells," *Sol. Energy Mater. Sol. Cells*, vol. 92, no. 7, pp. 686–714, Jul. 2008.
- [64] V. I. Madogni, B. Kounouhéwa, A. Akpo, M. Agbomahéna, S. A. Hounkpatin, and C. N. Awanou, "Comparison of degradation mechanisms in organic photovoltaic devices upon exposure to a temperate and a subequatorial climate," *Chem. Phys. Lett.*, vol. 640, pp. 201–214, Nov. 2015.
- [65] C. Tao *et al.*, "Performance improvement of inverted polymer solar cells with different top electrodes by introducing a MoO₃ buffer layer," *Appl. Phys. Lett.*, vol. 93, no. 19, p. 193307, Nov. 2008.
- [66] A. K. K. Kyaw, X. W. Sun, C. Y. Jiang, G. Q. Lo, D. W. Zhao, and D. L. Kwong, "An inverted organic solar cell employing a sol-gel derived ZnO electron selective layer and thermal evaporated MoO₃ hole selective layer," *Appl. Phys. Lett.*, vol. 93, no. 22, p. 221107, Dec. 2008.
- [67] R. Steim, S. A. Choulis, P. Schilinsky, and C. J. Brabec, "Interface modification for highly efficient organic photovoltaics," *Appl. Phys. Lett.*, vol. 92, no. 9, pp. 2006–2009, 2008.
- [68] N. Yeh and P. Yeh, "Organic solar cells: Their developments and potentials," *Renew. Sustain. Energy Rev.*, vol. 21, pp. 421–431, 2013.
- [69] P. W. M. Blom, V. D. Mihailetschi, L. J. A. Koster, and D. E. Markov, "Device physics of polymer:Fullerene bulk heterojunction solar cells," *Adv. Mater.*, vol. 19, no. 12, pp. 1551–1566, 2007.
- [70] C. J. Brabec *et al.*, "A low-bandgap semiconducting polymer for photovoltaic devices and infrared emitting diodes," *Adv. Funct. Mater.*, vol. 12, no. 10, pp. 709–712, 2002.
- [71] J. Piriš *et al.*, "Photogeneration and ultrafast dynamics of excitons and charges in P3HT/PCBM blends," *J. Phys. Chem. C*, vol. 113, no. 32, pp. 14500–14506, 2009.
- [72] S. Rafique, S. M. Abdullah, K. Sulaiman, and M. Iwamoto, "Fundamentals of bulk heterojunction organic solar cells: An overview of stability/degradation

- issues and strategies for improvement,” *Renew. Sustain. Energy Rev.*, vol. 84, no. November 2017, pp. 43–53, 2018.
- [73] J.-C. Ke, Y.-H. Wang, K.-L. Chen, and C.-J. Huang, “Effect of open-circuit voltage in organic solar cells based on various electron donor materials by inserting molybdenum trioxide anode buffer layer,” *Sol. Energy Mater. Sol. Cells*, vol. 133, pp. 248–254, Feb. 2015.
- [74] M. Song, J. Kim, S. Yang, and J. Kang, “Solution-processed silver nanowires as a transparent conducting electrode for air-stable inverted organic solar cells,” *Thin Solid Films*, vol. 573, pp. 14–17, 2014.
- [75] M. Chalh, S. Vedraïne, B. Lucas, and B. Ratier, “Solar Energy Materials & Solar Cells Plasmonic Ag nanowire network embedded in zinc oxide nanoparticles for inverted organic solar cells electrode,” *Sol. Energy Mater. Sol. Cells*, vol. 152, pp. 34–41, 2016.
- [76] A. Kojima, K. Teshima, Y. Shirai, and T. Miyasaka, “Organometal halide perovskites as visible-light sensitizers for photovoltaic cells,” *J. Am. Chem. Soc.*, vol. 131, no. 17, pp. 6050–6051, 2009.
- [77] J. H. Im, C. R. Lee, J. W. Lee, S. W. Park, and N. G. Park, “6.5% Efficient Perovskite Quantum-Dot-Sensitized Solar Cell,” *Nanoscale*, vol. 3, no. 10, pp. 4088–4093, 2011.
- [78] H. S. Kim *et al.*, “Lead iodide perovskite sensitized all-solid-state submicron thin film mesoscopic solar cell with efficiency exceeding 9%,” *Sci. Rep.*, vol. 2, no. 591, pp. 1–7, 2012.
- [79] W. S. Yang *et al.*, “Iodide management in formamidinium-lead-halide-based perovskite layers for efficient solar cells,” *Science (80-.)*, vol. 356, no. 6345, pp. 1376–1379, 2017.
- [80] Z. Song, S. C. Watthage, A. B. Phillips, and M. J. Heben, “Pathways toward high-performance perovskite solar cells: review of recent advances in organometal halide perovskites for photovoltaic applications,” *J. Photonics Energy*, vol. 6, no. 2, p. 022001, 2016.
- [81] I. Hussain, H. P. Tran, J. Jaksik, J. Moore, N. Islam, and M. J. Uddin, “Functional materials, device architecture, and flexibility of perovskite solar cell,” *Emergent Mater.*, vol. 1, no. 3–4, pp. 133–154, 2018.
- [82] L. Etgar *et al.*, “Mesoscopic CH₃NH₃PbI₃/TiO₂ heterojunction solar cells,” *J. Am. Chem. Soc.*, vol. 134, no. 42, pp. 17396–17399, 2012.
- [83] V. Gonzalez-Pedro *et al.*, “General working principles of CH₃NH₃PbX₃ perovskite solar cells,” *Nano Lett.*, vol. 14, no. 2, pp. 888–893, 2014.

- [84] S. A. Kulkarni, T. Baikie, P. P. Boix, N. Yantara, N. Mathews, and S. Mhaisalkar, "Band-gap tuning of lead halide perovskites using a sequential deposition process," *J. Mater. Chem. A*, vol. 2, no. 24, pp. 9221–9225, 2014.

